Research Article **Open Access**

Francesco Stoppa*, Claudia Principe, Mariangela Schiazza, Yu Liu, Paola Giosa, and Sergio Crocetti

Magma evolution inside the 1631 Vesuvius magma chamber and eruption triggering

DOI 10.1515/geo-2017-0003
Received Jan 19, 2016; accepted Sep 05, 2016

Abstract: Vesuvius is a high-risk volcano and the 1631 Plinian eruption is a reference event for the next episode of explosive unrest. A complete stratigraphic and petrographic description of 1631 pyroclastics is given in this study. During the 1631 eruption a phonolite was firstly erupted followed by a tephritic phonolite and finally a phonolitic tephrite, indicating a layered magma chamber. We suggest that phonolitic basanite is a good candidate to be the primitive parental-melt of the 1631 eruption. Composition of apatite from the 1631 pyroclastics is different from those of CO_2-rich melts indicating negligible CO_2 content during magma evolution. Cross checking calculations, using PETROGRAPH and PELE software, accounts for multistage evolution up to phonolite starting from a phonolitic basanite melt similar to the Vesuvius medieval lavas. The model implies crystal settling of clinopyroxene and olivine at 6 kbar and 1220°C, clinopyroxene plus leucite at a pressure ranging from 2.5 to 0.5 kbar and temperature ranging from 1140 to 940°C. Inside the phonolitic magma chamber K-feldspar and leucite would coexist at a temperature ranging from from 940 to 840°C and at a pressure ranging from 2.5 to 0.5 kbar. Thus crystal fractionation is certainly a necessary and probably a sufficient condition to evolve the melt from phono tephritic to phonolitic in the 1631 magma chamber. We speculate that phonolitic tephrite magma refilling from deeper levels destabilised the chamber and triggered the eruption, as testified by the seismic precursor phenomena before 1631 unrest.

Keywords: 1631 Vesuvius eruption; 1631 magma chamber; 1631 magma composition; apatite chemistry; Vesuvius parental melt; eruptive triggering

1 Introduction

Somma-Vesuvius historic activity is characterised by occasional Plinian eruptions (79 A.D., 472 A.D., 1631 A.D.) separated by long periods of inactivity [1]. Each Plinian eruption was followed by an open-conduit phase, producing either effusive, often eccentric, eruptions [2] or mixed (effusive and explosive) eruptions, of Strombolian to violent-Strombolian type and sub-plinian [3]. Plinian eruptions produced evolved pyroclastics ranging from phonolitic tephrite to tephritic phonolite [4]. In contrast, eccentric effusive vents poured out fluid phonolitic basanite or phonolitic tephrite lavas (as studied in this paper). This behaviour suggests differentiation in the magma chamber leading to the Plinian eruptions, as opposed to sudden discharge of near-primary magma rising from a deep reservoir. Both reactivation scenarios are needed to describe the volcanic hazard in the Vesuvius area.

A classical approach has been adopted here, with the deliberate omission of models generated by experiments using artificial charges. Hard data from rocks and minerals, collected through accurate stratigraphic work are used instead. Juvenile pyroclastic composition is used to constrain the possible parental magma, its liquid line of descent and chemical zoning in the magma chamber. Magma evolution software was used to verify the hypotheses created using the field and petrological data. With regards to the nomenclature of the rocks we use that approved by International Union of Geological Sciences [5].

All the hypotheses proposed for the Vesuvius Plinian eruptions are considered to explain the magma chamber evolution up to the triggering of the eruption: (I) fractional crystallisation and an increase in volatiles pressure leading to magma chamber wall breakage [6], (II) limestone Assimilation and Fractional Crystallisation (AFC) with con-

***Corresponding Author: Francesco Stoppa:** Dipartimento di Scienze Psicologiche, della Salute e del Territorio, Università G.d'Annunzio, Chieti-Pescara, Italy; Email: fstoppa@unich.it
Claudia Principe: Istituto di Geoscienze e Georisorse, CNR-Pisa, Italy
Mariangela Schiazza: Dipartimento di Scienze Psicologiche, della Salute e del Territorio, Università G.d'Annunzio, Chieti-Pescara, Italy
Yu Liu: College of Zijin Mining, Fuzhou University, China
Paola Giosa, Sergio Crocetti: Istituto di Geoscienze e Georisorse, CNR-Pisa, Italy; Dipartimento di Scienze della Terra, Università di Pisa, Italy

sequent explosion [7], (III) feeder dyke formation with the injection of fresh hot magma in the plumbing system and consequent destabilisation of the chamber [8, 9]; (IV) a combination of the above mechanisms [10].

The behaviour of volatiles, especially CO_2, which is particularly crucial in AFC models [7], has been investigated using apatite compositional variations.

The ultimate aim of this work is the formulation of a melt evolution model for the 1631 magma chamber and its eruption trigger, which represents one of the possible future hazardous scenarios in the case of explosive reactivation of the volcano [11]. This possible unrest has to be evaluated and forecast with maximum effort through a multidisciplinary approach, as the next Vesuvius eruption will impact one of the world most populated and vulnerable volcanic areas.

2 The 1631 AD eruption and deposits

The 1631 event is classified as a relatively small Plinian eruption [12] following both the approach of [6] based on the eruptive column height of about 20 km and with the discharge rate (M_0) peak of 8×10^7 kg/sec [13]. Before this eruption, Vesuvius was at rest for about five centuries [14]. The 1631 eruption caused more than 4,000 fatalities, significantly affected the Neapolitan region and influenced the evolution of natural sciences in the first half of the 17th century [15]. Due to the proximity of Vesuvius to Naples, this eruption was described in hundreds of contemporaneous chronicles. Long-term seismic precursors are documented and consist of several local events felt in Naples from 1616 to 1630, ranging on the Mercalli Cancani Sieberg (MCS) intensity scale from III to VII [16]. Notably two main seismic sequences are recorded during 1620 to 1622 and in 1626 with a damaging event that occurred on 10th March 1626 at 00:40 h (UT). In addition, on 2nd April 1630 Naples was rocked by a powerful quake described as fairly long and producing a considerable shaking of buildings [16]. In 1631, from November to December, considerable seismic activity occurred in the Vesuvius area culminating in a grade VII MCS shake on 15th December at 23:00 h (UT), followed by an intense seismic swarm (> 30 felt shocks) [16]. As a whole, two seismic swarms culminating in a grade VII MCS event occurred in the five years prior to the eruption. At the same time, short-term precursors, such as sensible ground-deformation, were accurately documented during the final week before the eruption [13, 14].

According to [13], the eruption started on 16th December 1631 at 07:00 h (UT) with the rapid growth of an eruptive column that lasted around 8 hours. Fallout of vesiculated lapilli and lithic clasts occurred until 18:00 (UT) on this day (Plinian phase). During the night between the 16th and 17th the volcano produced discrete explosions accompanied by lapilli relapses (Vulcanian phase). At 10:00 (UT) on December 17th several hot pyroclastic flows gushed out during a major collapse of the summit of Vesuvius (*Nuées Ardentes* phase). These flows travelled to the nearby coast in a few minutes, destroying everything in their path (Fig. 1a). Afterwards a column of ash arose from the large depression left after the *Nuées Ardentes* phase. In the night between the 16th and the 17th and in the following days extensive lahars and floods, resulting from heavy rains, affected the valleys of the volcano and spread across the plain North and Northeast of Vesuvius, producing further devastation. This eruptive sequence is not substantially different from that of the Plinian eruption of 79 A.D. [1]

The main depositional unit of the 1631 eruption consists of a thick Plinian fallout bank (Fig. 1b, Fig. 2c, 2d) composed of vesiculated white-greenish lapilli, crystals and lithic clasts, overlying a 30 cm thick paleosoil (Fig. 2d). At the mid-level of the fallout deposit there is a change in colour of the juvenile pyroclasts from white-greenish to grey-greenish (Fig. 2c). On this basis the Plinian fallout depositional unit is subdivided in two subunits: the "white fallout" and the "grey fallout" (Fig. 1b) [13]. This deposit has been sub-divided into seven layers (from *a* to *f* in Fig. 1b) on the basis of planar discontinuities, gradation, grain size and component changes. The crystal-rich *a* layer (Fig. 1b and Fig. 2d) corresponds to the early stage formation of the Plinian column. Layers *b*, *c*, and *d* form the "white" sub-unit. The layer *d* is a mixed level with light- and dark-pumices, while the "grey" sub-unit is comprised of e_i, e_s, and *f* layers. The *f* layer shows a large amount of lithic clasts and high-density lapilli. In the fallout-type sections of Scudieri and San Leonardo (2 and 8 in Fig. 1a), the Plinian fallout is overlain by a few centimetres of lapilli deposited during the Vulcanian phase (*g* layer in Fig. 1b).

The pyroclastic rocks produced by the *Nuées Ardentes* phase confined to the higher slopes of Somma-Vesuvius were emplaced by diluted density currents (surges) [13]. Concentrated pyroclastic density currents (pyroclastic flows) entered the valleys of the southern portion of the volcano and spread through the foothill areas into the sea (Fig. 1a) [13, 17]. The pyroclastic flows are up to 8 m thick, unwelded, massive and ash-rich, characterised by notable amounts of lava lithic clasts, clinopyroxene adcumulates, skarn fragments, and marls. Occasionally sparse remains

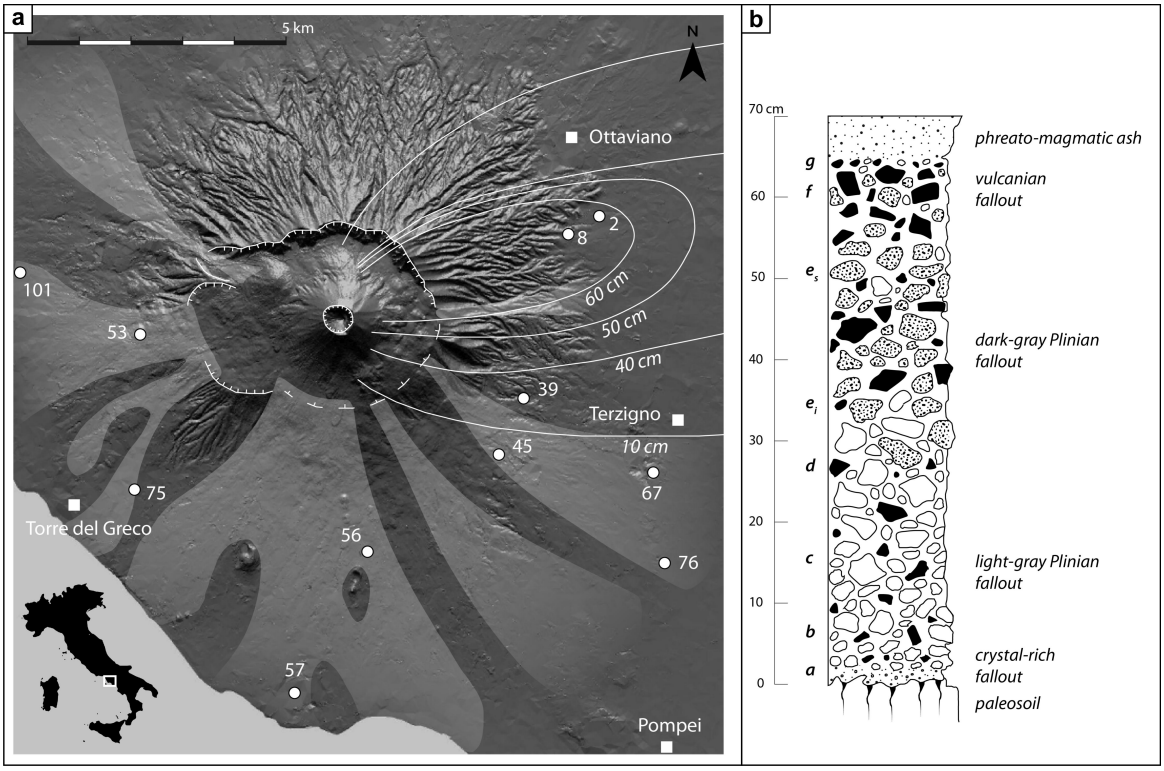

Figure 1: (a) Sketch map of 1631 eruption deposits. Distribution on the ground of the Plinian fallout emitted on 16th December 1631 (isopach contour lines in white) and areas affected by the pyroclastic flows emitted on the morning of 17th December 1631 during the *Nuées Ardentes* phase (transparent white areas) (modified from [13]). Numbered white spots refer to the sampling sites described in Table 1. Plinian fallout distribution is due to Westerly winds and consequently accumulated the East of the volcano. Due to the presence of the Monte Somma north of the Vesuvius main cone, pyroclastic flows mainly flowed and accumulated in the southern portion of the volcano Surge deposits distribution is not shown. (b) Stratigraphical column of the 1631 fallout deposits subdivided into two subunits (grey and white), on the base of the colour changes inside the deposit. To assess different eruptive phases, which may correspond to different conditions of magma emission, changes of composition and of volatile content in the chamber, a fine distinction of fallout deposit in several layers (*a-f*) was conducted on the type-sections of Scudieri (2) and San Leonardo (8). The fallout sequence is topped by the phreatomagmatic ashes emitted at the end of the eruption, after the collapse of Vesuvius main cone. The *g* layer corresponds to the vulcanian fallout emitted during the night of December 16th.

of charred vegetation are found (Fig. 2b). In some localities (*e.g.*, Pozzelle quarry) (site 45 in Fig. 1a) up to four flow-units are present (Fig. 2a and 2b).

3 Methods

3.1 Sampling

Fallout deposits were mainly sampled in the two type-sections of San Leonardo and Scudieri (respectively 8 and 2; Fig. 1a). Samples were collected from each one of the seven layers composing the fallout deposit (Table 1). Sampling was repeated in two different sections to obtain robust data on chemical variation inside the fallout deposit. A total of 69 single juvenile scorias from pyroclastic flow units were handpicked and analysed (Table 1). Assuming that the Plinian fallout deposit is fully representative of the magma chamber conditions prior to the eruption, as demonstrated by the bulk rock geochemistry (section 3.2), apatite chemistry of 10 samples from the Plinian fallout were analysed (Table 3a). Apatite crystals, about 0.01 mm long, were separated by heavy liquid (sodium polytungstate) settling, purified using Frantz magnetic separators at different operative conditions and finally handpicked.

3.2 Bulk rock analyses

Representative juvenile components were crushed and powdered and used for major and trace elements analyses. Seventy-nine whole-rock chemical analyses were performed at Actlabs Laboratories, Canada via inductively

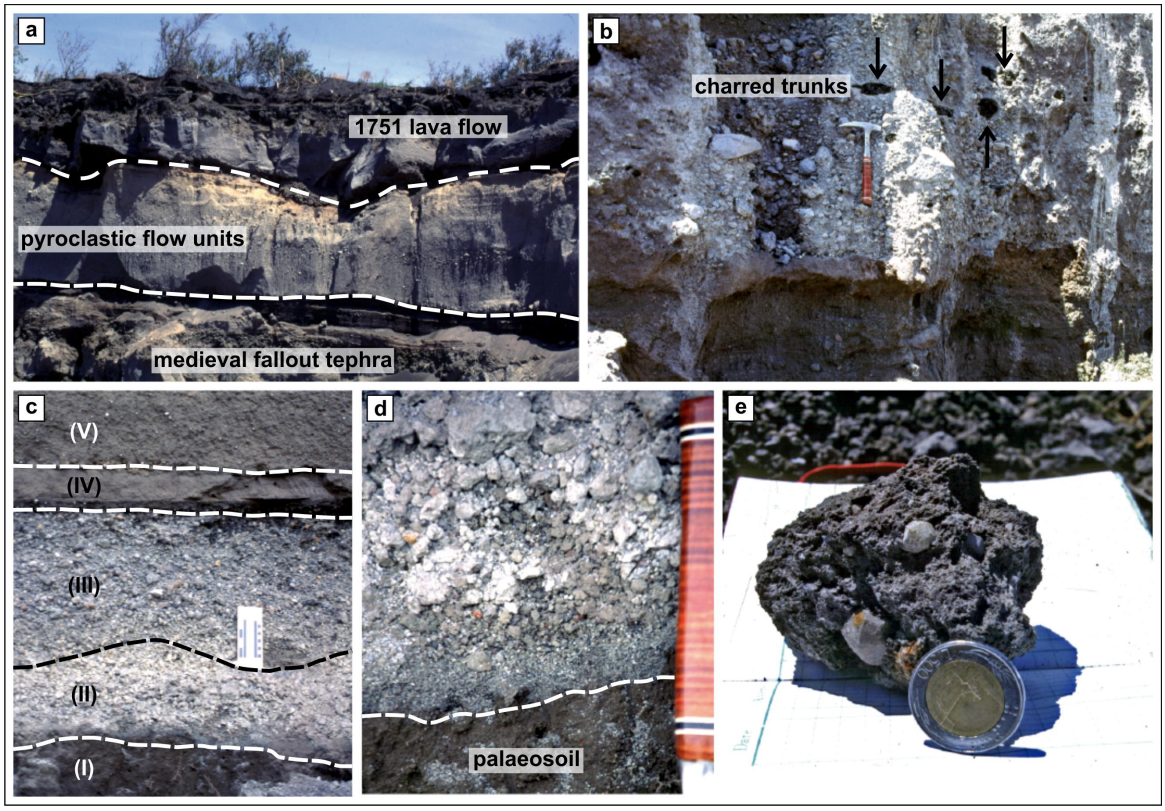

Figure 2: Field exposures in quarries where fresh juvenile components of 1631 deposits were collected. (a) In the site of Pozzelle quarry a medieval fallout tephra at the bottom and the lava flow of the 1751 eruption at top, constrain four flow units of the 1631 pyroclastic flow. (b) Detail of the lower part of the basal pyroclastic flow unit in Fig. 2a. The black spots above the hammer are sections of charred tree trunks. (c) (I) Paleosoil, (II), light-gray scoriae fallout (III), dark-gray scoriae fallout, (IV) phreatomagmatic ashes fallout deosit, (V) lahar deposit. (d) Crystal-rich fallout (fine grained) at contact with the paleosoil, marked by a white dashed line. (e) Discrete bomb showing large euhedra of leucite, the coin shown in the picture has a diameter of 26 mm.

coupled plasma mass spectrometry (ICP-MS). A set of CO_2 determinations was obtained by Othmer-Fröhlich method at the Institute of Geosciences and Georesources, CNR-Pisa. Fluorine was determined by NaOH fusion and specific ion electrode, Cl was determined by water leaching and ICP-MS. Instrumental sensitivity for major elements is 0.01%, and between 0.01 and 1 ppm for trace elements. Reproducibility is between 2% and 5% for major elements and 2% for most of the trace elements. Data in Table 2a, 2b are rounded to three figures in accordance with instrumental sensitivity.

3.3 Scanning Electron Microscope (SEM) and Electron Micro Probe Analysis (EMPA)

Apatite crystals were preliminarily examined using an Energy Dispersive System (EDS) on a SEM, then were analysed for Ca, Sr, Fe, Mg, Mn, Na, La, Ce, Nd, Y, P, Si, S, F and Cl with a Cameca Sx50 microprobe run at 15 kV and 20 nA, at the London Natural History Museum (EMMA division) using wollastonite as a standard for Ca and Si, synthetic Sr and Ti oxide for Sr, pure metals for Fe and Mn, olivine for Mg, jadeite for Na, rare earth glass for Ce, La, Nd, Y, Durango apatite for P and F, celestite for S and halite for Cl. As F analysis may result in count acceleration [18], P and F were analysed with short counting times at the beginning of the analytical sequence. After data collection for the major elements, longer measurements were made for the minor and trace elements, since this second group of elements shows less variation with beam exposure time. The apatite formula $A_{10}(XO_4)_6(OH,F,Cl)_2$ was adopted.

3.4 X-ray diffraction for determination of lattice parameters (XRDSC), Infra Red (IR) and Raman

Selected single apatite crystals were investigated by XRDSC. IR and Raman spectroscopic investigations were

Table 1: Sampling list showing sampling site position with reference to Fig. 1a, stratigraphical position and sample label of bulk rock and separate apatite.

Sampling site #	Distance from the crater (km)	Azimut	Locality		Eruptive unit	Juvenile sample name	Apatites
45	4.2	N130°E	Pozzelle quarry		1st pyroclastic flow unit	F45PS	
					3rd and 4th pyroclastic flow unit	GIO7	
53	3.8	N267°E	San Vito-Ercolandia		pyroclastic flow unit	F53J	
67	6.5	N116°E	Mauro Vecchio quarry		pyroclastic flow unit	F67PS	
75	5	N230°E	Torre del Greco-Viale della Gioventù		pyroclastic flow unit	F75PS	
76	7.7	N128°E	Passanti quarry		pyroclastic flow unit	F76PS	
57	7.3	N183°E	Villa Inglese quarry		pyroclastic flow unit	GIO5	
101	6.3	N275°E	Portici Cemetery		pyroclastic flow unit	GIO9	
56	4.5	N173°E	Cappella Nuova-New road behind Viulo cone		pyroclastic flow unit	GIO6	
2	4.6	N69°E	Scudieri quarry	**g**	vulcanian fallout	TIL2-g	**2g**
				f	Plinian fallout layer	TIL2-f	**2f**
				es	Plinian fallout layer	TIL2-es	**2es**
				es	Plinian fallout layer	TIL2-esD	
				ei	Plinian fallout layer	TIL2-ei	**2ei**
				d	Plinian fallout layer	TIL2-dS	**2d**
				c	Plinian fallout layer	TIL2-cS	
				b	Plinian fallout layer	TIL2-b	**2b**
				a	Plinian fallout layer	TIL2-a	**2a**
39	3.5	N115°E	Pastino-Azienda Agricola Fabbricini		dark-gray Plinian fallout subunit	TIL39-N	**39n**
					light-gray Pliniana fallout subunit	TIL39-B	**39b**
8	5.4	N70°E	Barri-San Leonardo		dark greenish-gray subunit	TIL8-N	**8n**
				f	Plinian fallout layer	TIL8-fD	
				f	Plinian fallout layer	GIO10-f	
				f	Plinian fallout layer	GIO11-f	
				es	Plinian fallout layer	GIO10-es	
				es	Plinian fallout layer	GIO11-es	
				es	Plinian fallout layer	GIO12-es	
				es	Plinian fallout layer	TIL8-esS	
				ei	Plinian fallout layer	TIL8-ei	
				ei	Plinian fallout layer	GIO12-ei	
				ei	Plinian fallout layer	GIO11-ei	
				ei	Plinian fallout layer	GIO10-ei	
				d+c	Plinian fallout layer	GIO10-c+d	
				d+c	Plinian fallout layer	GIO11-c+d	
				d+c	Plinian fallout layer	GIO12-c+d	
				d	Plinian fallout layer	TIL8-dS	
				c	Plinian fallout layer	TIL8-cS	
				b	Plinian fallout layer	GIO10-b	
				b	Plinian fallout layer	GIO11-b	
				b	Plinian fallout layer	GIO12-b	

performed to detect the volatile-related components in the structure, such as CO_3^{2-}, SO_4^{2-}, F^-, Cl^- and OH^-. Lattice parameters were determined by a four-circle X-ray diffractometer (radiation MoKα, graphite-monochromatised). About 50 reflections were adopted to calculate the parameters using a LAT program of Phillips with an estimated error lower than 0.001Å. The *a* and *c* cell parameters are listed in Table 3a and depicted in Fig. 4a-4c. The IR spectra using a KBr disc were scattered in a Fourier Transform IR instrument Bruker mod. IFS113V, collecting 50–100 scans

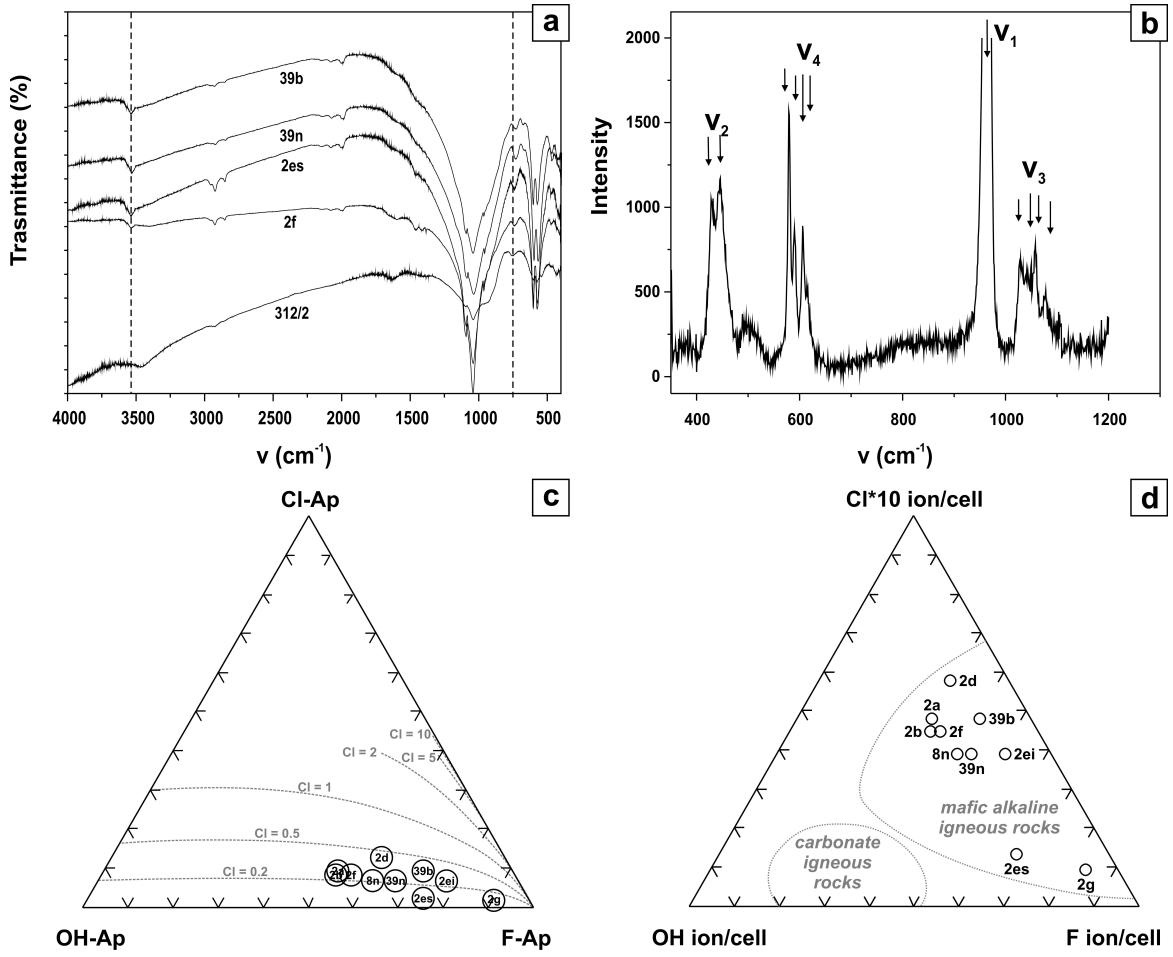

Figure 3: (a) Infra Red Spectra and (b) Raman spectra of 1631 apatite samples; (c) and (d) triangular plots showing the molar fractions of the apatite end-members, hydroxyapatite (OH-Ap) and fluorapatite (F-Ap): (c) molar contents are compared with various igneous trends of low Cl apatite after [20]; (d) molar contents indicate affinity of 1631 apatites with alkaline mafic rock and exclude affinity with melts containing CO_2 or CO_3^- [25].

in vacuum (P = 5 mbar) over the range 400–4000 cm^{-1}. The oriented micro-Raman spectrum sample 39b was measured using a 180-degree back-scattering geometry with a Labram micro-spectrometer (instrument mod S.A.). A curve-fitting program was applied for the determination of frequencies of the weak bands for both IR and Raman spectra.

4 Mineralogy of 1631 apatite

4.1 Apatite geochemistry

Owing to its particular crystal-chemical properties, apatite structure allows a number of substitutions at different sites. During fractional crystallisation the melt enriches in volatiles, such as H_2O, H_2S, SO_2, CO_2, HF and HCl, as the corresponding ionic species, OH^-, S^{2-}, SO_4^{2-}, CO_3^{2-}, F^-, and Cl^- are not incorporated into the lattice of crystallising solid phases. Some of these ionic species (*e.g.*, OH^-, CO_3^{2-}, F^- and Cl^-) can easily enter the apatite structure [19, 20]. Consequently, the compositional evolution of apatites mimics that of the magma from which they crystallised. In particular, the substitution among the F^-, Cl^- and OH^- ions, which occupy the structural channel (Z site), is a sensitive indicator of the fugacity of corresponding volatiles in the magma [21, 22]. So, co-variations in apatite ionic species (*e.g.*, OH^-, Cl^-, F^-) related to volatile components (*e.g.*, H_2O, HCl, HF) and non-volatile elements (*e.g.*, Rare Earth Elements (REEs)) in the magma suggest that a common process (*e.g.*, fractional crystallisation) occurs during apatite crystallisation (Fig. 4a-4c). In addition, apatite is crucial to assess CO_2 content in the crystallising melt.

4.2 XRDSC and Vibrational spectroscopy

Vibrational Spectra of the 1631 apatite samples clearly show the OH absorption bands at 3540 cm^{-1} (stretching mode) and in the region of 725–750 cm^{-1} (libration mode), in agreement with the OH content obtained from formula calculations (Fig. 3a). By IR we find the difference between Fap and OH-bearing Ap and classified it to F-Hap. However, OH content is estimated by difference in channel site, assuming F + OH + Cl = 2 [23, 24]. Based on the EMPA data, the tetrahedral sites are fully occupied by phosphate ions in the 1631 samples and there is no evidence for the presence of carbonate ions. Accordingly, in the Raman spectra of the studied samples, only PO_4 vibrational bands at 961 (ν_1), 471–474 (ν_2), 1040–1090 (ν_3) and 566–604 cm^{-1} (ν_4) can be resolved and there are no carbonate bands. For example, in the representative Raman spectrum of sample 39b (Fig. 3b), one ν_1 peak at 964 cm^{-1}, two ν_2 peaks at 430 and 446 cm^{-1}, four ν_3 peaks at 1029, 1048, 1059, and 1078 cm^{-1} and four ν_4 peaks at 580, 590, 607, and 616 cm^{-1} were resolved, similar to those of the apatite end members [25]. Finally, Si and S contents of the 1631 samples should be less than 1% because it is not possible to resolve peaks related to structural SiO_4, SO_4, CO_3 anions by these Raman spectra.

4.3 EMPA

In the 1631 apatites the A-site is chiefly filled by Ca with a slight substitution of Mg, Sr and light REEs (less than 0.1 apfu), while the X-site is mainly occupied by P with a weak substitution of Si and S (generally less than 0.1 apfu). The most distinctive substitution occurs in the channel, with F varying from 1.05 to 1.82 apfu, Cl from 0.02 to 0.24 apfu and OH from 0.16 to 0.80 apfu (Table 3a).

4.4 Apatite data implications

Apatites from the vent-opening deposit levels (sample 2a in Fig. 3c, d and Table 3a) and the first emitted Plinian fallout pumices (sample 2b in Fig. 3c, 3d and Table 3a) have the lowest molar fraction of F-Ap, and the highest OH-Ap values, whereas apatites from the Vulcanian phase deposit (sample 2g in Fig. 3c, 3d, Table 3a) have the highest F-Ap and the lowest OH-Ap fraction (Fig. 3c). The molar fractions of F-Ap and OH-Ap change quite regularly along the sequence, except for sample 2f, which shows lower F-Ap and higher OH-Ap than adjacent samples, consistent with its probable formation position at the con-

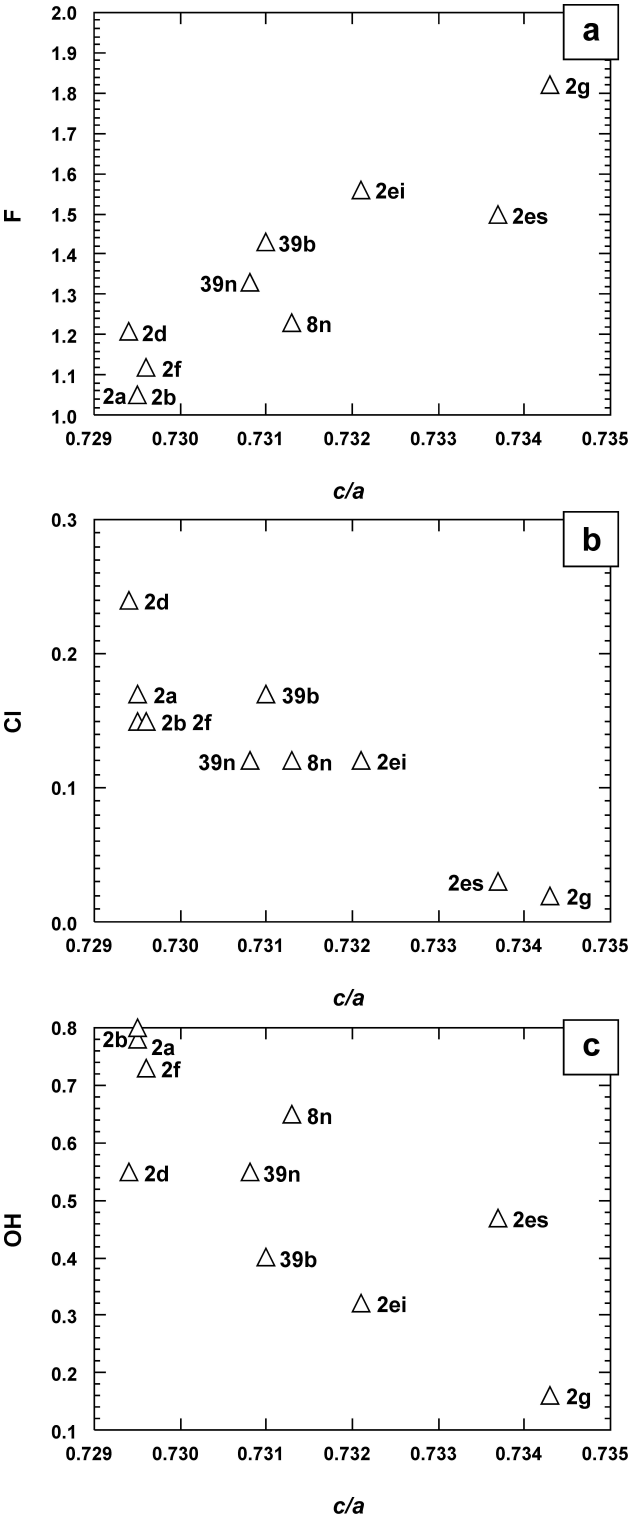

Figure 4: *a* and *c* cell parameter ratio variation compared with (a) fluorine, (b) chlorine and (c) oxydril content a.p.f.u. Note a progressive semi-regular increasing of *c/a* along the eruptive sequence directly correlated to F increase and inversely correlated with Cl and OH.

Table 2a: Representative bulk rock analysis and normative calculation for 1631 pyroclastic rocks and historical Vesuvius lavas. (a) Major oxides and petrological indices and (b) trace elements.
Basanites at Vesuvius are represented by two medieval lava flows, while the last column refer to the average of Mediterranean basanites (data from literature). Detection limits for Vesuvius analyses are 0.01%, 0.05 and 0.1 ppm, for major oxides and trace elements, respectively. The error of these analyses is < 1% for major elements, except Na, LOI and CO_2, where the total error amounts to ca. 3%; for trace elements, total error amounts to ca. 2% for concentration > 300 ppm, 5% for concentrations of 50 to 300 ppm and > 10% for concentrations < 20 ppm.

	PHONOLITE (white lapilli)					TEPHRITIC PHONOLITE (white lapilli)				
Sample	**GIO5B**	**GIO5C**	**F67PS(2)**	**BD1**	**F67PS(5)**	**BGIO12/B**	**GIO6L**	**F67PS(6)**	**F67PS(3)**	**F75P(3)S**
	(a)	(a)	(a)	(b)	(a)	(b)	(a)	(a)	(a)	(a)
SiO_2 (wt.%)	49.9	51.0	52.3	52.7	53.4	48.4	49.5	50.9	51.5	52.0
TiO_2	0.53	0.52	0.65	0.55	0.53	0.66	0.68	0.70	0.62	0.66
Al_2O_3	19.9	20.3	19.6	19.6	20.4	18.2	18.6	19.0	19.4	19.1
FeO*	4.54	4.45	5.12	5.13	4.51	5.16	5.30	5.40	4.94	5.13
MnO	0.13	0.13	0.13	0.13	0.13	0.13	0.13	0.13	0.13	0.12
MgO	1.23	1.19	1.17	1.24	1.29	2.44	2.77	2.88	2.20	2.58
CaO	5.81	5.81	7.46	5.64	6.18	7.98	7.92	8.43	7.47	7.89
Na_2O	4.10	4.14	4.28	4.39	4.43	3.77	3.88	3.60	3.94	3.68
K_2O	9.35	9.71	7.36	8.28	7.57	7.06	7.82	7.15	7.98	6.69
P_2O_5	0.20	0.16	0.39	0.20	0.23	0.37	0.42	0.44	0.34	0.41
BaO	0.27	0.28	0.28	0.27	0.28	0.26	0.27	0.28	0.29	0.28
SrO	0.10	0.11	0.11	0.12	0.12	0.12	0.10	0.11	0.11	0.11
LOI	3.40	1.70	1.22	1.77	1.13	4.70	1.70	1.08	1.24	1.40
Total	99.5	99.5	100	100	100	99.3	99.2	100	100	100
Cl	279	439	264	n.a.	151	239	434	499	233	381
F	2080	2120	1450	n.a.	2320	2210	1750	1870	1980	2010
Mg#	0.33	0.32	0.29	0.30	0.34	0.46	0.48	0.49	0.44	0.47
S.I.	6.40	6.11	6.53	6.51	7.25	13.2	14.0	15.1	11.5	14.3
CIPW norm										
or	27.0	26.9	44.2	49.6	45.4	29.1	23.6	33.9	34.6	40.2
ab	0.0	0.0	0.9	0.0	4.9	0.0	0.0	0.0	0.0	4.0
an	8.7	8.3	12.6	9.5	13.5	12.7	10.6	14.6	11.7	16.1
lc	24.2	25.2	0.0	0.4	0.0	11.9	18.9	7.0	10.4	0.0
ne	19.6	19.5	19.4	20.5	17.9	18.3	18.3	16.7	18.3	15.0
wo	8.5	8.5	9.5	7.5	6.8	11.3	11.4	10.5	10.0	8.9
en	2.5	2.5	2.5	2.1	2.1	4.7	5.0	4.7	4.0	3.8
fs	6.3	6.4	7.4	5.8	5.0	6.6	6.4	5.8	6.1	5.1
fo	0.5	0.4	0.3	0.8	0.8	1.2	1.5	1.9	1.1	1.9
fa	1.3	1.1	1.0	2.4	2.2	1.9	2.1	2.6	1.8	2.8
mt	0.0	0.0	0.0	0.0	0.0	0.0	0.0	0.0	0.0	0.0
he	0.0	0.0	0.0	0.0	0.0	0.0	0.0	0.0	0.0	0.0
il	1.1	1.0	1.3	1.1	1.0	1.3	1.3	1.4	1.2	1.3
ap	0.5	0.4	0.9	0.5	0.5	0.9	0.9	1.0	0.8	0.9
Total	100	100	100	100	100	100	100	100	100	100
de La Roche's index										
R1	−457	−482	85	−140	75	77	−70	274	12	436
R2	1074	1079	1240	1050	1125	1333	1350	1417	1288	1347
Rm	1074	1079	1240	1050	1125	1333	1350	1417	1288	1347
Rs	1999	2033	2304	2239	2340	2138	2133	2318	2241	2421
Ri	2455	2515	2219	2379	2265	2061	2203	2044	2229	1985

note: (a) = Pyroclastic flow; (b) = Plinian fallout; (c) = Lava; FeO* = total iron; n.a. = not analyzed; ** = http://georoc.mpch-mainz.gwdg.de/georoc/

Continued on next page

Table 2a: Representative bulk rock analysis and normative calculation for 1631 pyroclastic rocks and historical Vesuvius lavas. (a) Major oxides and petrological indices and (b) trace elements.
Basanites at Vesuvius are represented by two medieval lava flows, while the last column refer to the average of Mediterranean basanites (data from literature). Detection limits for Vesuvius analyses are 0.01%, 0.05 and 0.1 ppm, for major oxides and trace elements, respectively. The error of these analyses is < 1% for major elements, except Na, LOI and CO_2, where the total error amounts to ca. 3%; for trace elements, total error amounts to ca. 2% for concentration > 300 ppm, 5% for concentrations of 50 to 300 ppm and > 10% for concentrations < 20 ppm.

	PHONOLITIC TEPHRITE (drak-grey lapilli)						PHONOLITIC BASANITES		
Sample	**AGIO12/Ei**	**DGIO12/B**	**BGIO12/Es**	**GV2**	**TILES(4)D**	**F76PS(1)**	**PA10**	**PA28**	**avg.**
	(b)	(b)	(b)	(a)	(b)	(a)	(c)	(c)	**193****
SiO_2 (wt.%)	45.9	46.6	47.5	48.7	48.3	49.4	48.4	47.6	42.5
TiO_2	0.83	0.82	0.82	0.85	0.88	0.70	0.97	1.00	2.89
Al_2O_3	16.4	17.0	17.1	15.7	17.2	18.0	13.3	13.7	13.2
FeO*	5.80	5.85	5.78	6.82	6.05	5.32	7.15	7.04	11.1
MnO	0.13	0.13	0.13	0.13	0.13	0.12	0.14	0.13	0.18
MgO	4.55	4.22	4.68	5.82	5.42	4.58	8.13	7.77	10.1
CaO	10.42	10.41	10.70	11.16	11.36	9.41	12.88	12.83	11.4
Na_2O	3.07	3.17	2.87	2.52	2.66	3.38	2.57	1.55	3.60
K_2O	6.42	6.72	6.82	5.95	6.15	7.01	3.83	5.35	1.59
P_2O_5	0.68	0.63	0.69	0.72	0.77	0.55	0.72	0.76	0.87
BaO	0.23	0.24	0.23	0.23	0.29	0.29	0.12	0.15	0.07
SrO	0.10	0.10	0.10	0.08	0.09	0.11	0.06	0.06	0.08
LOI	4.80	3.30	2.00	1.13	0.70	1.23	0.80	1.20	1.90
Total	99.3	99.2	99.4	99.8	100	100	99.0	99.1	99.5
Cl	122	169	231	n.a.	276	293	n.a.	n.a.	n.a.
F	2160	2420	2150	n.a.	1790	1950	n.a.	n.a.	n.a.
Mg#	0.58	0.56	0.59	0.60	0.61	0.61	0.67	0.66	0.62
S.I.	22.9	21.1	23.2	27.6	26.7	22.6	37.5	35.8	38.3
CIPW norm									
or	6.2	5.1	7.2	17.1	11.9	18.9	19.2	8.2	9.8
ab	0.0	0.0	0.0	0.0	0.0	0.0	0.0	0.0	7.9
an	12.6	12.9	13.9	14.1	17.0	13.4	13.7	14.9	15.9
lc	26.8	28.6	27.0	14.7	19.5	18.2	3.1	19.0	0.0
ne	14.9	15.2	13.6	11.7	12.3	15.7	12.0	7.3	12.9
wo	15.9	15.6	15.3	15.8	14.8	12.8	19.7	19.1	15.9
en	8.4	8.0	8.2	8.6	8.2	7.0	11.8	11.4	13.7
fs	7.0	7.3	6.6	6.7	6.0	5.4	6.8	6.7	0.0
fo	2.6	2.2	2.7	4.4	3.8	3.3	6.2	6.0	8.9
fa	2.4	2.2	2.4	3.7	3.1	2.8	4.0	3.9	0.0
mt	0.0	0.0	0.0	0.0	0.0	0.0	0.0	0.0	0.6
he	0.0	0.0	0.0	0.0	0.0	0.0	0.0	0.0	12.4
il	1.7	1.6	1.6	1.6	1.7	1.4	1.9	1.9	0.0
ap	1.6	1.4	1.6	1.6	1.7	1.2	1.6	1.7	2.0
Total	100	100	100	100	100	100	100	100	100
de La Roche's index									
R1	284	221	367	746	644	285	1189	1146	999
R2	1661	1657	1712	1790	1822	1587	2042	2027	1706
Rm	1662	1657	1712	1790	1822	1587	1231	2027	1985
Rs	2114	2119	2210	2411	2350	2256	2101	2512	2228
Ri	1830	1898	1843	1665	1705	1971	2175	1366	1122

note: (a) = Pyroclastic flow; (b) = Plinian fallout; (c) = Lava; FeO* = total iron; n.a. = not analyzed; ** = http://georoc.mpch-mainz.gwdg.de/georoc/

Concluded

Table 2b: Representative bulk rock analysis and normative calculation for 1631 pyroclastic rocks and historical Vesuvius lavas. (a) Major oxides and petrological indices and (b) trace elements.
Basanites at Vesuvius are represented by two medieval lava flows, while the last column refer to the average of Mediterranean basanites (data from literature). Detection limits for Vesuvius analyses are 0.01%, 0.05 and 0.1 ppm, for major oxides and trace elements, respectively. The error of these analyses is < 1% for major elements, except Na, LOI and CO_2, where the total error amounts to ca. 3%; for trace elements, total error amounts to ca. 2% for concentration > 300 ppm, 5% for concentrations of 50 to 300 ppm and > 10% for concentrations < 20 ppm.

	PHONOLITE (white lapilli)					TEPHRITIC PHONOLITE (white lapilli)				
Sample	**GIO5B**	**GIO5C**	**F67PS(2)**	**BD1**	**F67PS(5)**	**BGIO12/B**	**GIO6L**	**F67PS(6)**	**F67PS(3)**	**F75P(3)S**
	(a)	(a)	(a)	(b)	(a)	(b)	(a)	(a)	(a)	(a)
Ba (ppm)	1772	1828	1842	1738	1837	1702	1762	1856	1867	1811
Rb	332	353	294	267	282	254	304	274	304	294
Sr	1000	1078	1106	1176	1183	1161	921	1091	1091	1057
Y	24.0	25.0	27.0	24.0	26.0	24.8	25.2	28.0	25.0	25.0
Zr	261	272	258	182	280	218	250	254	254	247
Nb	50.6	53.4	51.0	51.0	58.0	43.4	40.9	46.0	49.0	46.0
Th	33.9	35.3	32.4	n.a.	37.5	28.6	29.4	30.0	30.8	28.9
Pb	56.0	57.0	27.0	n.a.	64.0	41.0	24.0	46.0	54.0	47.0
Ga	18.9	19.6	17.5	n.a.	18.1	17.0	17.5	17.1	17.1	17.8
Zn	64.0	66.0	44.0	n.a.	73.0	68.0	60.0	61.0	64.0	65.0
Cu	25.0	21.0	32.0	n.a.	29.0	32.0	36.0	40.0	39.0	49.0
Ni	10.0	10.0	17.0	6.0	6.0	10.0	10.0	22.0	16.0	20.0
V	124	127	142	131	122	143	160	160	145	156
Cr	13.7	6.8	24.0	10.0	10.0	41.1	27.4	37.0	22.0	31.0
Hf	4.4	4.5	5.1	n.a.	5.1	4.7	4.7	5.0	4.8	4.6
Cs	23.1	24.8	18.0	n.a.	16.6	16.3	20.3	15.9	17.8	19.5
Sc	3.0	3.0	9.0	n.a.	4.0	8.0	10.0	11.0	8.0	9.0
Ta	2.8	2.9	2.7	n.a.	3.1	2.5	2.4	2.4	2.6	2.5
Co	9.8	9.9	15.0	12.0	13.0	15.0	15.0	19.0	16.0	17.0
U	13.8	14.2	12.6	n.a.	15.0	11.3	10.7	11.6	11.8	10.6
W	5.0	6.0	12.0	n.a.	5.0	6.0	14.0	4.0	5.0	7.0
Sn	2.0	2.0	3.0	n.a.	2.0	8.0	3.0	3.0	2.0	4.0
Mo	5.0	5.0	4.0	n.a.	5.0	4.0	5.0	5.0	5.0	5.0
Tl	1.0	0.8	0.3	n.a.	0.3	0.3	0.7	0.3	0.3	0.6
As	11.0	9.0	3.0	n.a.	13.0	14.0	1.0	10.0	9.0	18.0
Cd	0.1	0.1	0.1	n.a.	0.1	0.1	0.1	0.1	0.1	0.1
Sb	0.7	0.3	0.3	n.a.	0.5	0.5	0.3	0.3	0.3	0.3
Bi	0.6	0.7	0.3	n.a.	0.3	0.7	0.6	0.5	0.6	0.3
La	69.0	71.3	70.0	79.0	70.0	60.7	63.0	69.0	66.0	65.0
Ce	128	129	109	140	125	122	118	126	121	109
Pr	13.7	13.9	14.2	n.a.	14.3	13.7	13.5	14.0	13.3	13.0
Nd	47.5	47.9	52.4	n.a.	51.4	53.0	50.2	53.1	48.9	51.1
Sm	8.9	8.7	9.6	n.a.	9.1	9.5	9.4	9.6	9.0	8.4
Eu	2.0	2.1	2.3	n.a.	2.2	2.2	2.2	2.4	2.1	2.3
Gd	6.1	6.3	7.0	n.a.	6.6	6.7	6.9	7.2	6.6	6.4
Tb	0.8	0.9	1.0	n.a.	0.9	0.9	0.9	1.0	0.9	0.9
Dy	4.8	4.9	5.2	n.a.	5.0	5.1	5.1	5.2	5.0	4.7
Ho	0.8	0.8	0.9	n.a.	0.9	1.0	0.9	0.9	0.9	0.8
Er	2.5	2.6	2.7	n.a.	2.7	2.4	2.6	2.7	2.6	2.4
Tm	0.3	0.3	0.3	n.a.	0.4	0.4	0.3	0.3	0.3	0.3
Yb	2.2	2.3	2.4	n.a.	2.5	2.3	2.2	2.4	2.3	2.1
Lu	0.3	0.3	0.4	n.a.	0.4	0.3	0.3	0.3	0.3	0.3

Continued on next page

Table 2b: Representative bulk rock analysis and normative calculation for 1631 pyroclastic rocks and historical Vesuvius lavas. (a) Major oxides and petrological indices and (b) trace elements.
Basanites at Vesuvius are represented by two medieval lava flows, while the last column refer to the average of Mediterranean basanites (data from literature). Detection limits for Vesuvius analyses are 0.01%, 0.05 and 0.1 ppm, for major oxides and trace elements, respectively. The error of these analyses is < 1% for major elements, except Na, LOI and CO_2, where the total error amounts to ca. 3%; for trace elements, total error amounts to ca. 2% for concentration > 300 ppm, 5% for concentrations of 50 to 300 ppm and > 10% for concentrations < 20 ppm.

Sample	PHONOLITIC TEPHRITE (drak-grey lapilli)						PHONOLITIC BASANITES		
	AGIO12/Ei	**DGIO12/B**	**BGIO12/Es**	**GV2**	**TILES(4)D**	**F76PS(1)**	**PA10**	**PA28**	**avg.**
	(b)	(b)	(b)	(a)	(b)	(a)	(c)	(c)	**193****
Ba (ppm)	1496	1545	1506	1523	1905	1876	1375	1656	730
Rb	244	235	283	220	243	270	n.a.	228.3	99.0
Sr	1001	1004	968	814	908	1020	758	791	901
Y	26.5	25.3	25.3	23.0	27.0	27.0	23.0	23.1	28.0
Zr	213	211	197	151	221	243	150	142	449
Nb	35.3	36.2	33.0	28.0	34.0	43.0	21.0	21.4	138
Th	24.8	24.3	23.6	n.a.	22.4	27.2	n.a.	11.7	15.3
Pb	35.0	34.0	34.0	n.a.	36.0	48.0	n.a.	11.0	8.3
Ga	17.6	16.5	16.5	n.a.	16.8	17.1	n.a.	13.9	22.0
Zn	58.0	60.0	51.0	n.a.	49.0	65.0	78.0	32.0	101
Cu	45.0	42.0	54.0	n.a.	63.0	46.0	73.0	68.0	37.2
Ni	95.0	35.0	36.0	48.0	44.0	25.0	98.0	68.0	110
V	184	177	184	195	194	175	n.a.	233	183
Cr	95.8	75.3	75.3	100	71.0	41.0	226	205	208
Hf	4.4	5.2	4.6	n.a.	4.8	5.0	n.a.	4.0	6.6
Cs	16.0	15.1	18.2	n.a.	14.5	17.0	n.a.	12.0	0.9
Sc	16.0	15.0	16.0	n.a.	22.0	14.0	35.0	35.0	17.2
Ta	2.2	2.1	2.1	n.a.	2.0	2.4	<20	1.1	4.1
Co	22.8	21.1	23.4	26.0	23.0	19.0	36.0	31.9	43.1
U	9.3	9.4	8.7	n.a.	8.1	10.0	n.a.	5.5	n.a.
W	6.0	5.0	4.0	n.a.	5.0	6.0	n.a.	5.0	n.a.
Sn	3.0	7.0	3.0	n.a.	5.0	4.0	n.a.	2.0	n.a.
Mo	4.0	4.0	4.0	n.a.	4.0	6.0	n.a.	2.1	n.a.
Tl	0.5	0.2	0.6	n.a.	0.2	0.2	n.a.	<0.1	n.a.
As	13.0	12.0	12.0	n.a.	9.0	22.0	n.a.	9.0	n.a.
Cd	0.1	0.1	0.1	n.a.	0.1	0.1	n.a.	<0.2	n.a.
Sb	0.5	0.7	0.3	n.a.	0.5	1.5	n.a.	<0.5	n.a.
Bi	0.3	0.3	0.3	n.a.	0.8	0.7	n.a.	<0.5	n.a.
La	57.9	58.0	54.8	59.0	64.0	63.0	n.a.	37.2	67.6
Ce	119	116	111	103	104	120	80.0	67.1	118
Pr	14.0	13.8	13.4	n.a.	13.5	13.6	n.a.	9.2	11.7
Nd	57.3	54.3	52.5	n.a.	54.9	54.8	n.a.	41.0	46.2
Sm	11.2	9.9	10.4	n.a.	9.6	9.0	n.a.	7.7	8.4
Eu	2.5	2.4	2.4	n.a.	2.6	2.5	n.a.	2.2	2.4
Gd	7.6	7.4	7.6	n.a.	7.5	7.0	n.a.	6.9	6.9
Tb	1.0	1.0	1.0	n.a.	1.0	0.9	n.a.	1.0	1.0
Dy	5.2	5.5	5.1	n.a.	5.2	5.1	n.a.	4.5	5.2
Ho	1.0	0.9	0.9	n.a.	0.9	0.9	n.a.	0.8	1.0
Er	2.7	2.7	2.5	n.a.	2.6	2.5	n.a.	2.0	2.5
Tm	0.3	0.4	0.3	n.a.	0.3	0.3	n.a.	0.3	0.3
Yb	2.5	2.3	2.1	n.a.	2.2	2.2	n.a.	2.0	2.2
Lu	0.4	0.3	0.3	n.a.	0.3	0.3	n.a.	0.3	0.3

Concluded

tact with the skarn shell of the magma chamber. On the other hand, there is no significant co-variation of Cl-Ap with stratigraphic position. The variation of *a* and *c* cell parameters, together with the *c/a* ratio, are characteristic

of OH-F binary apatites (Table 3a and 3b). Only F, Cl and OH are meaningful in terms of correlation with *c/a* with magmatic evolution along the eruptive sequence (4 a, b and c). According to [25], who established chemical characteristics for apatites from different alkaline rocks and carbonatites, the 1631 compositions, in terms of F-Cl-OH, are typical of mafic alkaline silicate rocks and are clearly different from those of apatites crystallising from CO_2-rich melts (Fig. 3d). Summing up, the chemistry of 1631 apatites excludes their crystallisation from either a CO_3^{2-}-saturated melt or a carbonate-contaminated melt and highlight a general increase of volatiles (such as OH) from the bottom to the top of the magma chamber, which is coherent with a fractional crystallisation process.

5 Petrology

5.1 Juvenile lapilli petrography

Juvenile lapilli of the 1631 eruption are vesiculated, showing a porphyritic texture in which there is a continuous variation in crystal size (*i.e.*, seriate texture) (Fig. 5a) and variable mineral phases/glass ratios, with crystal content between 20 and 36 vol.% [13].

Lapilli pheno-modal composition is generally leucite phonolitic tephrite but many samples show clearly that K-feldspar dominates on plagioclase and are leucite tephritic phonolite or even phonolite. Phonolitic tephrite samples contain more abundant leucite and magnetite. Main phases are: glass (44.0–74.0 vol.%), clinopyroxene (5.6–34.1 vol.%), leucite + (nepheline) (3.7–12.2 vol.%), plagioclase (2.0–9.5 vol.%), mica (0.7–9.1 vol.%), K-feldspar (0.4–5.4 vol.%), magnetite (0.4–3.2 vol.%), apatite (0.5–2.6 vol.%), garnet (0.4–0.7 vol.%) and olivine (1.0–2.0%). A feldspatoid of the cancrinite group (microsommite) was also observed [13]. K-feldspar forms corroded skeletal or euhedral phenocrysts (Fig. 5c). Larger corroded crystals show kaolinitic alteration along cleavages, with faint zonation and/or perthites. Abundant, euhedral fresh K-feldspar laths are in the groundmass. Plagioclase is zoned, generally subhedral and forms seriate phenocrystals. Leucite is generally fresh, euhedral in the groundmass with concentric magnetite inclusion, or forms large fragments up to 2 cm (Fig. 2e), showing characteristic sector polysynthetic twinning and K-feldspar and clinopyroxene inclusions (Fig. 5b). Nepheline is limited to small intergranular patches. Clinopyroxene occurs as large subhedral or euhedral zoned crystals, showing corrosion features, whereas smaller groundmass clinopyroxene crystals have skeletal features. Biotite-phlogopite flakes show kink bending and fringed endings. Some large mica crystals show corrosion and reaction rims, which indicate a possible xenocrystic origin. Mica contains abundant clinopyroxene and is possibly disaggregated from larger ultramafic nodules of mica-clinopyrossenite (Fig. 5d). Olivine forms small subhedral grains in the ground mass or rare resorbed phenocrysts. EMPA of olivine testifies

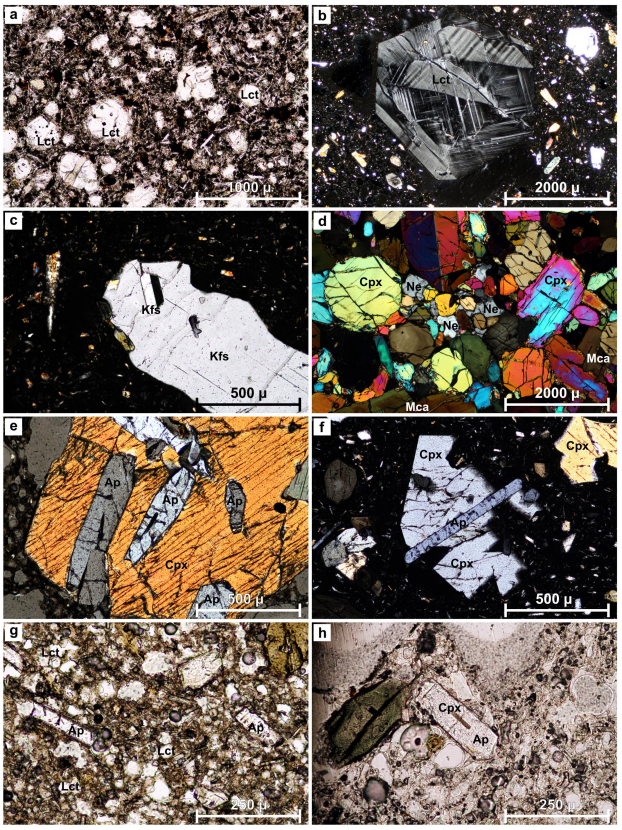

Figure 5: Alkaline rocks have a distinctive mineral assemblage and texture, which is used as a crucial criterion for their classification. The 1631 Vesuvius juvenile component shows an association of large phenocrysts of leucite in a ground mass composed of leucite, diospide and K-feldspars typical of many other Italian rocks of the high potassium (HK) series. (a) Leucite phonolitic tephrite: euhedral leucite in a groundmass of plagioclase, K-feldspar and clinopyroxene laths, magnetite and melanite garnet (// polars). (b) Details of a leucite crystal showing sector twinning (x polars). (c) Large, corroded, K-feld encasing a fresh euhedral crystal showing Carlsbad twinning (x polars). (d) Mica, nepheline clinopyroxenite, note triple junctions among clynopyroxene crystals indicating high-pressure crystallisation conditions (x polars). Apatite is often enclosed in silicate minerals, which prevented further reaction or requilibration with evolving magmatic liquid. (e) Several apatite euhedra included in clinopyroxene (x polars). (f) Long apatite crystals associated with corroded clinopyroxene (x polars). (g) Late-stage apatite represented by discrete crystals in the groundmass. (h) Clinopyroxene inclusions in groundmass apatite (// polars).

Table 3a: (a) Apatite analysis. Typical detection limits are in the order of 0.02 wt %. Each column represents the mean of two, and in one case of four and five analyses. Data reported are the mean values of repeated (in brackets) analyses on the same selected single crystals; (b) Olivine analysis.

Sample	2a(2)	2b(2)	2d(2)	2ei(2)	2es(2)	2f(2)	2g(4)	8n(2)	39b(2)	39n(5)
CaO	55.7	55.6	55.0	55.1	55.2	55.3	55.7	55.4	54.7	55.3
SrO	0.27	0.24	0.59	0.38	0.30	0.22	0.53	0.45	0.38	0.34
FeO	0.27	0.22	0.20	0.20	0.13	0.29	0.11	0.18	0.21	0.23
MgO	0.31	0.29	0.11	0.06	0.01	0.29	0.02	0.10	0.10	0.17
MnO	0.06	0.04	0.06	0.06	0.05	0.06	0.01	0.05	0.05	0.05
Na_2O	0.05	0.02	0.09	0.06	0.06	0.08	0.04	0.06	0.10	0.04
La_2O_3	0.14	0.08	0.14	0.10	0.13	0.11	0.17	0.17	0.15	0.16
Ce_2O_3	0.15	0.00	0.14	0.11	0.15	0.08	0.08	0.12	0.12	0.10
Nd_2O_3	0.09	0.04	0.07	0.02	0.07	0.05	0.08	0.06	0.06	0.06
Y_2O_3	0.04	0.01	0.04	0.08	0.01	0.06	0.06	0.02	0.03	0.04
P_2O_5	41.1	41.0	41.2	41.2	39.9	41.2	41.0	41.1	40.8	41.2
SiO_2	0.64	0.50	0.52	0.61	0.47	0.47	0.56	0.48	0.50	0.54
SO_3	0.50	0.35	0.33	0.53	0.03	0.33	0.23	0.30	0.34	0.27
F	2.02	2.01	2.30	2.95	2.84	2.14	3.46	2.34	2.68	2.53
Cl	0.62	0.53	0.84	0.41	0.10	0.54	0.07	0.42	0.58	0.43
H_2Ocal	0.71	0.72	0.49	0.29	0.42	0.66	0.14	0.59	0.36	0.49
O=F+Cl	0.99	0.97	1.16	1.34	1.22	1.02	1.47	1.08	1.26	1.16
Total	101.7	100.6	100.9	100.8	98.7	100.9	100.7	100.7	99.8	100.8
atoms per formula unit (a.p.f.u.)										
Ca	9.820	9.870	9.820	9.870	9.900	9.810	9.900	9.860	9.850	9.850
Sr	0.020	0.020	0.060	0.040	0.030	0.020	0.050	0.040	0.040	0.030
Fe	0.040	0.030	0.030	0.030	0.020	0.040	0.020	0.020	0.030	0.030
Mg	0.070	0.070	0.030	0.010	0.000	0.070	0.000	0.020	0.020	0.040
Mn	0.010	0.000	0.010	0.010	0.010	0.010	0.000	0.010	0.010	0.010
Na	0.020	0.010	0.030	0.020	0.020	0.020	0.010	0.020	0.030	0.010
LREE	0.020	0.010	0.030	0.020	0.020	0.020	0.020	0.020	0.020	0.020
P	5.720	5.740	5.810	5.830	5.660	5.780	5.750	5.770	5.800	5.810
Si	0.110	0.080	0.090	0.100	0.080	0.080	0.090	0.080	0.080	0.090
S	0.060	0.040	0.040	0.070	0.000	0.040	0.030	0.040	0.040	0.030
F	1.050	1.050	1.210	1.560	1.500	1.120	1.820	1.230	1.430	1.330
Cl	0.170	0.150	0.240	0.120	0.030	0.150	0.020	0.120	0.170	0.120
OH	0.780	0.800	0.550	0.320	0.470	0.730	0.160	0.650	0.400	0.550
Lattice parameters										
a (Å)	9.4176	9.4179	9.4255	9.3989	9.389	9.4169	9.3791	9.4074	9.4093	9.4088
c (Å)	6.8698	6.8708	6.8745	6.8805	6.889	6.8707	6.8874	6.879	6.8779	6.8762
c/a	0.7295	0.7295	0.7294	0.7321	0.7337	0.7296	0.7343	0.7313	0.7310	0.7308
V (Å^3)	527.645	527.756	528.893	526.371	525.912	527.636	524.681	527.852	527.337	527.151

mafic glass and apatite inclusions but not carbonate inclusions. Garnet is present as small euhedral crystals immersed in the groundmass. It shows red-brown polarisation colours and slight birefringence typical of Ti-rich garnet melanite. Apatite occurs as an inclusion in clinopyroxene (Fig. 5e, 5f) and K-feldspar, or as discrete euhedral crystals in the groundmass (Fig. 5g) up to 250–300 μm showing clinopyroxene inclusions (Fig. 5h). Magnetite forms discrete euhedral crystals or crystal aggregates in the groundmass. Glass is clear, colourless to brown-yellow.

Table 3b: (a) Apatite analysis. Typical detection limits are in the order of 0.02 wt %. Each column represents the mean of two, and in one case of four and five analyses. Data reported are the mean values of repeated (in brackets) analyses on the same selected single crystals; (b) Olivine analysis.

Sample	SiO_2	TiO_2	$Al2O_3$	FeO	MnO	MgO	CaO	NiO	Cr_2O_3	Mg#
46Br1a #1	40.47	0.02	0.05	4.27	0.35	53.77	0.95	0.00	0.01	0.96
46Br1a #2	40.91	0.00	0.04	4.19	0.31	53.80	0.74	0.03	0.00	0.96
46Br1a #3	40.53	0.01	0.01	4.29	0.32	54.02	0.73	0.00	0.01	0.96

5.2 Skarns lithic fragments

Skarns are an interesting part of the lithic clasts from the 1631 eruption and sometimes show multiple complex contacts among igneous rock, skarn and marble (Fig. 6). The marble is medium-grained, quite pure periclase/brucite marble (Fig. 6a). The skarns are banded and their contact with porphyritic tephritic phonolite is marked by a phlogopite and/or clinopyroxene reaction rim, 1–10 mm thick (Fig. 6a). The skarn bands consist of millimetre-thick alternating undulated or convolute lamination of essential forsterite, spinel and calcite, roughly parallel to the boundaries of the magmatic rock rim (Fig. 6b). Skarn blocks vary from sharp fragmental shape to rounded corroded shapes infiltrated by the melt (Fig. 6c). A detailed mineralogical description of these skarns is found in [26, 27]. Observation of composite igneous, skarn and marble contacts in the 1631 ejecta testifies the very limited thickness of the skarn shell.

5.3 Bulk rock geochemistry

All 1631 rocks are generally silica under-saturated and have a potassic character. White lapilli (tephritic phonolite to phonolite) have an average SiO_2 content of 50.4 wt.%, up to a maximum of 53.4 wt.%. Grey lapilli (phonolitic tephrite) are always SiO_2-undersaturated with minimum SiO_2 of 44.9 wt.% and average of 48.1 wt.%. Notable differences in average major oxides characterises tephritic phonolite with respect to phonolitic tephrite lapilli: TiO_2 is 0.66 and 0.82 wt.%, Al_2O_3 is 18.8 and 16.7 wt.%, MgO is 2.60 and 4.93 wt.%, CaO is 7.76 and 10.7 wt.%, respectively, while Na_2O+K_2O is 11.4 (12.7 in the phonolitic samples) and 9.12 wt.% and P_2O_5 is 0.41 and 0.66 wt.%, respectively. The CO_2 content of most samples is below detection limit (< 0.1 vol.%) apart from two samples whose CO_2 concentration is between 0.5 and 0.7 vol.%, corresponding to 0.2–0.3 wt.% $CaCO_3$. In fact, very small fragments of sedimentary limestone are present as accidental lithics in the pyroclastic rocks that cannot be completely removed. SO_3 contents are generally less than 0.5 wt.%.

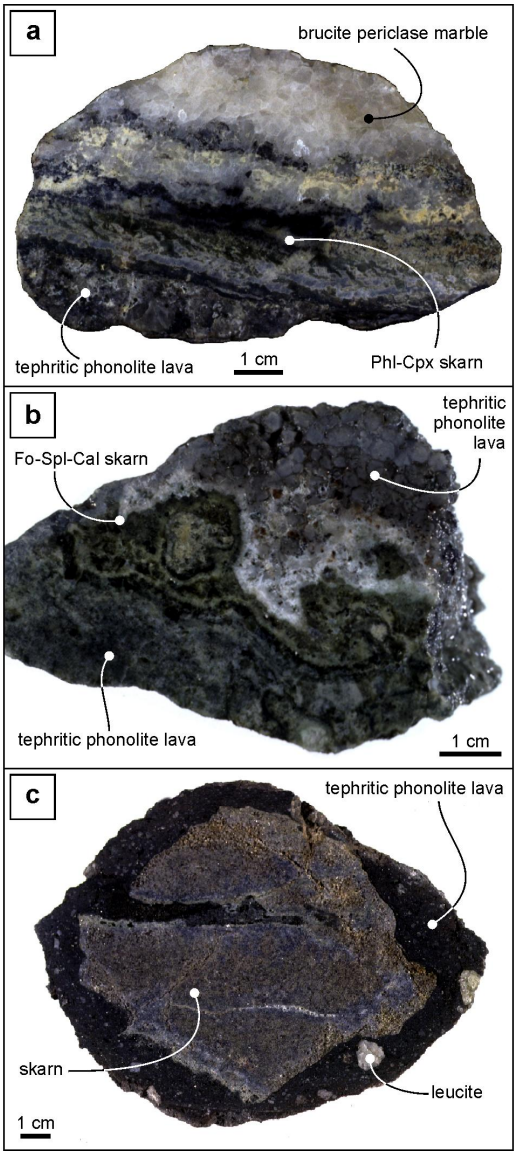

Figure 6: (a) Skarn block showing the contact between tephritic phonolite lava, phlogopite-clinopyroxese skarn and brucite-periclase marble. (b) Convolute contact between lava and skarn. Skarn shows layering of forsterite, spinel and calcite. (c) Angular skarn block in lava showing signs of corrosion and melt embayment.

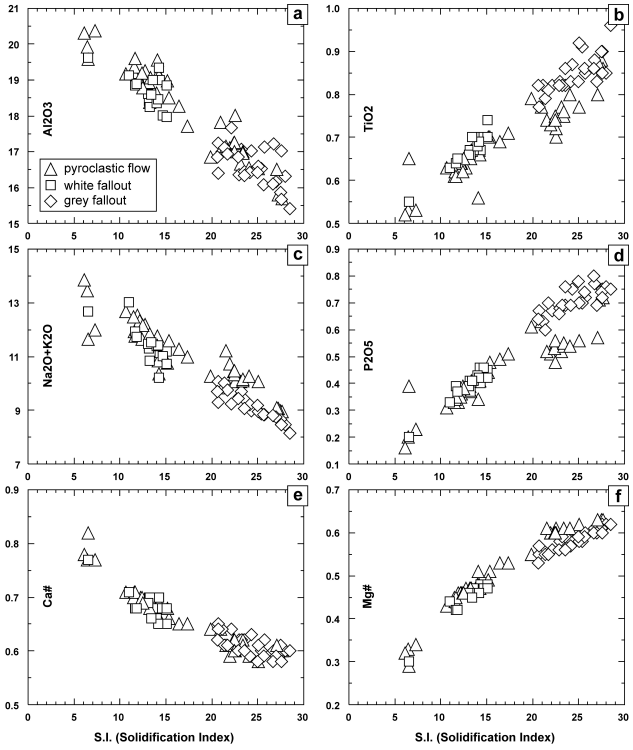

Figure 7: (a)–(f). Harker's diagrams illustrating major element variation vs. Solidification Index (S.I. = 100 * MgO / [MgO + FeO + Fe_2O_3 + Na_2O + K_2O) [28]. Felsic rocks have a low S.I. and mafic rocks have high S.I. Symbols refer to volcanological occurrence. Three chemical rock types are clearly apparent.

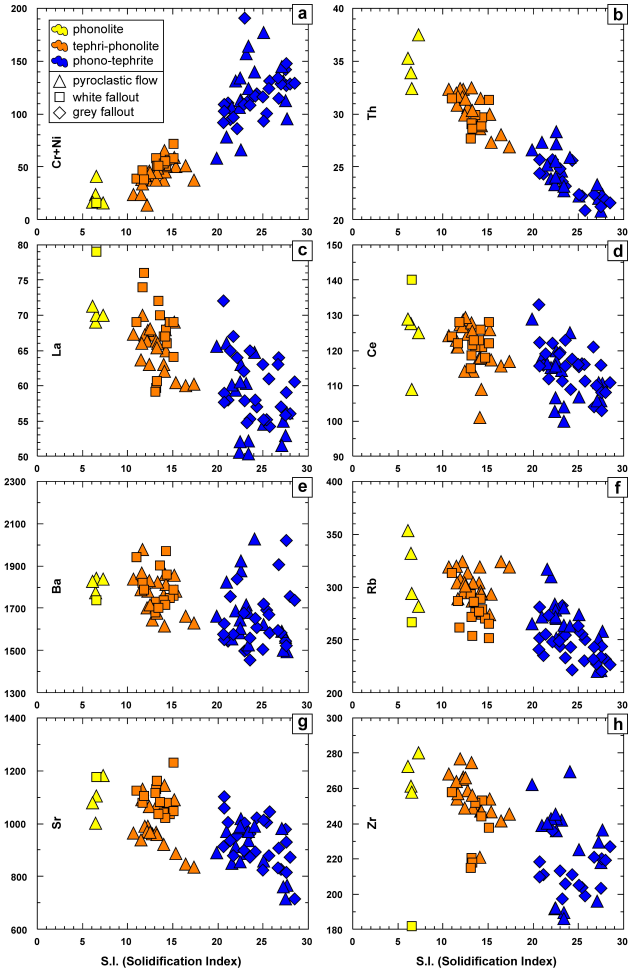

Figure 8: (a)–(h). Various Harker's diagrams illustrating trace element variation vs. Solidification Index [28]. Symbols colors refer to the chemical composition of the pyroclasts.

A general picture of major and trace element variations is depicted by their covariance with the solidification index (S.I. = 100 [MgO / (MgO + FeO + Fe_2O_3+ Na_2O + K_2O)]) of [28] (Fig. 7a–7f, Fig. 8a–8h). The solidification index is preferred in this context to the more commonly used SiO_2 or Mg# index [Mg / (Mg + Fe^{2+})], because the S.I. explains a much larger proportion of chemical variance, consequently highlighting the possible addition, if any, of external Ca and Mg (limestone) to the "magmatic" component.

Juvenile fragments from pyroclastic flows show a bimodal composition virtually identical to the light and dark lapilli in the Plinian fallout. Notably, in the white lapilli there is a more evolved sample that detaches from the rest in all the diagrams but compares with four lapilli samples from the pyroclastic flow samples (Fig. 7a–7f; Fig. 8a–8h). Although these evolved samples are ca. 5% of the dataset, data are consistent enough to justify a different rock-type (Fig. 9).

In the Total Alkali vs. Silica (TAS) diagram (Fig. 9a), the 1631 rock samples are somewhat dispersed in four different classification fields but most samples plot in the phono tephrite and tephri phonolite plotting fields. Several 1631 pyroclastics have water content > 2% and the use of the TAS diagram it is not advisable above this threshold [5]. Classification cannot simply be done based on the TAS diagram and a double check is required. The de La Roche's classification diagram is a neat addition and offers more value because its suitability for volatile-rich and alkaline rocks [29] (Fig. 9b). In addition, it has the two-fold advantage of being semi-normative and able to explain a much larger chemical variance as it involves all the major oxides and carbon [29]. Chemical composition of the 1631 rocks in the de La Roche diagram follows a narrow path basanite → tephrite → phonolitic tephrite → phonolite. In addition, this diagram shows that the tephrite and phonolitic tephrite compositions are pretty well separated and basanite and phonolite compositions are also represented.

Normative calculation (CIPW) (Table 2a) for 1631 samples provides additional information determining the

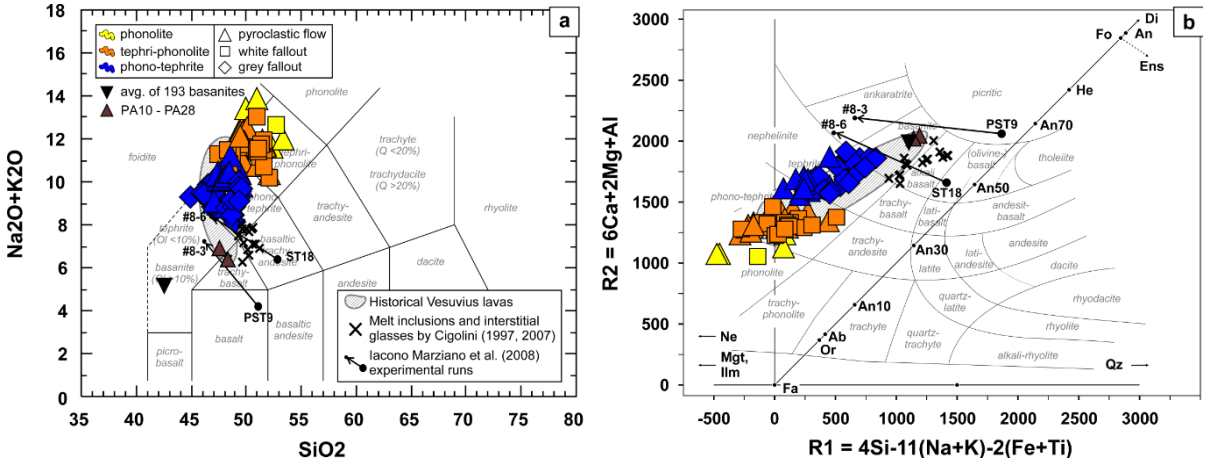

Figure 9: 1631 rocks and reference rocks plotting in (a) TAS (total alkali silica) and (b) in the semi-modal de La Roche's diagram [29], R1–R2 (R1 = 4Si-11(Na + K)-2(Fe + Ti); R2 = 6Ca + 2Mg + Al) Historical general trend of Vesuvius lavas (shaded area) is based on 89 analyses (Authors' unpublished data). The arrows link initial charge composition to final run obtained by adding about 15–17 wt.% of carbonate and 7–11et.% of olivine, respectively and 1 wt.% of H_2O [7].

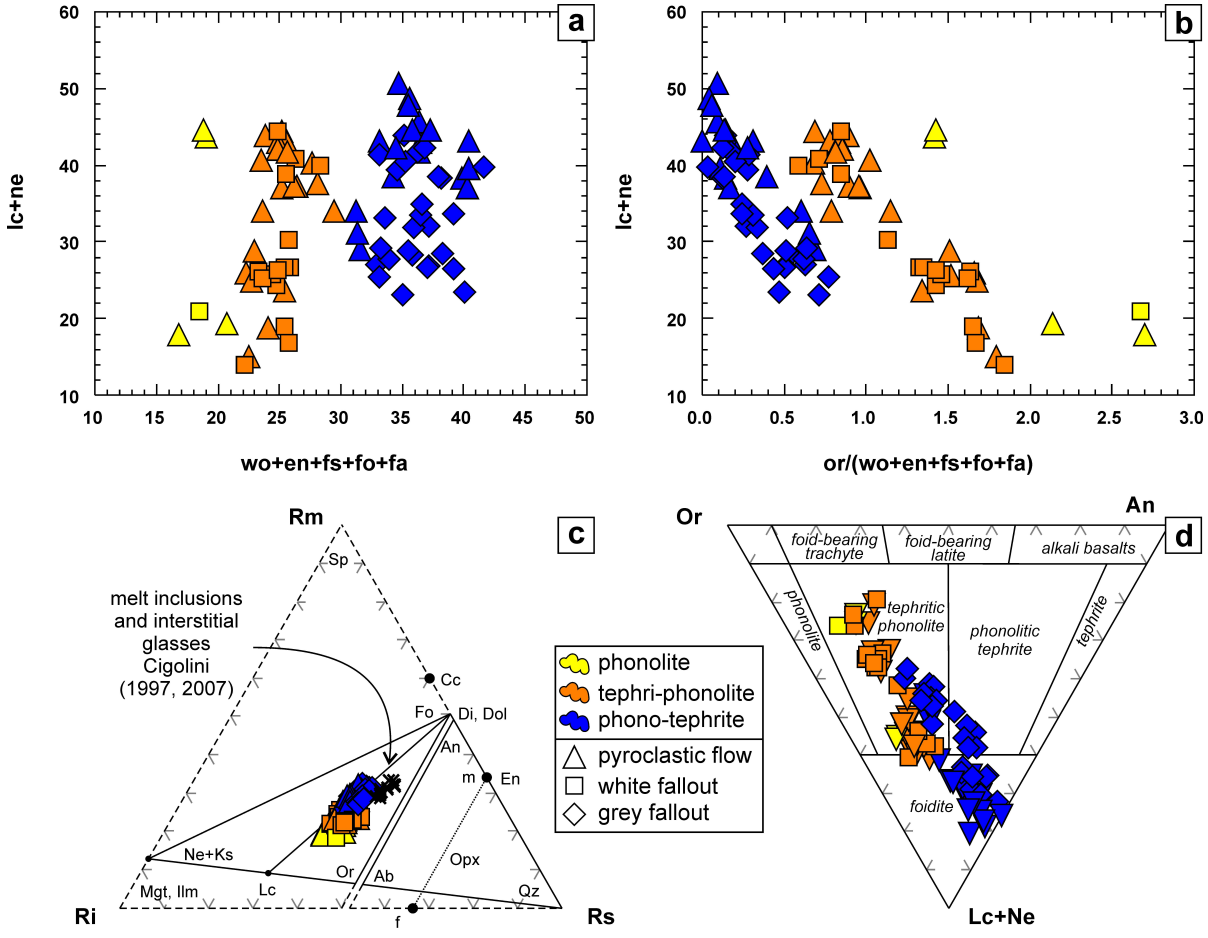

Figure 10: (a)–(d) CIPW normative discriminative diagrams. (a) and (b) normative variation of foids vs. mafic normative composition and foids variation vs. felsic/mafic normative component ratios; (c) Rm-Ri-Rs de la Roche's diagram (Rm = Al + 6Ca + 2Mg; Ri = 2[Fe + Ti] + 7[Na + K]; Rs = 4[Si + C-Na-K]) [29]; (d) Streckeisen's triangular plot. Data from Table 2a.

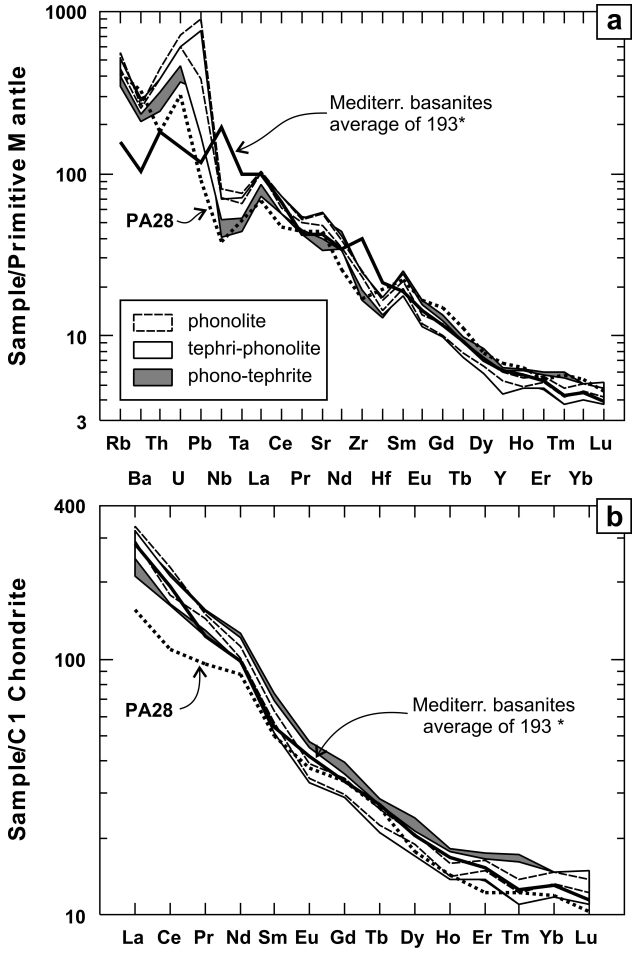

Figure 11: (a) and (b). Multi-element diagrams for 1631 juvenile components normalised to primitive mantle and CH1 chondrite [67]. Average basanite composition from anorogenic gelogical setting is displayed for comparison with the 1631 rocks [32]. PA28 is a Medieval Vesuvius lava of basanitic composition. Note a similar HFSE distribution and a strong enrichment of LILE in Vesuvius rocks in Fig. 11. REE distribution is very similar for 1631 rocks and average Mediterrean basanites, which have a lower LREE/HREE ratio, notably PA28 Vesuvious basanite shows a markedly lower LREE/HREE.

ideal mineralogy of these porphyritic rocks. The degree of silica saturation produces lc + ne saturation and abundant diopside formation. About 50% of the samples express some normative olivine, from 1.2% to 10.2% with an average of 4.2%, whereas modal olivine ranges from only 1 to 2%. Normative or + ab / wo + en + fs + fo + fa ratio works as a differentiation index and when plotted against normative lc + ne indicates that compositions with higher mafic content, for each rock types, correspond to the less evolved rocks having higher foids content (Fig. 10a, 10b). From a normative point of view, the 1631 samples are well defined in the Fo–(Ne + Ks)–Or triangle of the Rm–Rs–Ri diagram (Fig. 10c) [29]. More primitive compositions plot in the Fo–(Ne + Ks)–Lc sub-triangle but most compositions move towards Lc–Or tie-line in the Fo–Lc–Or sub-triangle. When the CIPW norms of 1631 samples are plotted in the conventional alkali feldspar - quartz - plagioclase - foids (AQPF) normative diagram (Fig. 10d), they spread from foidite (virtually Or-free) to tephritic phonolite. In general, normative diagrams are consistent with chemical classification and indicate a Fo-bearing composition (tephrite or basanite) evolving to an Or-rich term (phonolite). Combining chemical, normative and modal compositions, the following classification for the 1631 rocks types is adopted: leucite phonolitic tephrite, leucite tephritic phonolite and leucite phonolite. Phonolitic basanites are excluded upon [5] criteria because modal olivine is << 10 vol.% in the 1631 samples.

In tephritic phonolite and phonolitic tephrite, Ba averages 1778 and 1652 ppm, Sr averages 1035 and 921 ppm and the Cr + Ni sum averages 70.2 and 104 ppm, respectively. General chemical evolution of the melt is obtained by plotting large lithophile Elements (LILE) and high field strength elements (HFSE) vs. solidification index (Fig. 8). A considerable decrease in the Cr + Ni sum coupled with a significant increase in Th and La, Zr and especially incompatible Rb is apparent (Fig. 8). Again three different chemical rock-types are defined.

The most primitive 1631 samples TILES(4)D has MgO = 5.42 wt.%, $Mg_{\#}$ = 78 and Cr + Ni = 123 ppm. These values are comparable with those reported in the literature for the 1631 most primitive sample, GV2, from [45] that contains MgO = 5.82 wt.%, $Mg_{\#}$ = 77 and Cr + Ni = 148 ppm (Table 2a and 2b).

The most primitive Vesuvius rocks may be represented by medieval lavas PA10 or PA28 that have MgO = 7.77–8.01 wt.%, $Mg_{\#}$ = 67–83 and Cr + Ni = 273–324 ppm and normative olivine (Fo + Fa) ~ 10% (Table 2a and 2b). Representative Vesuvius basanite (PA28) displays higher LILE but lower Zr-Hf and Ta-Nb with respect to selected Mediterranean rocks classified as basanites in both the TAS and de La Roches's diagrams and having ~10% of olivine in the CIPW norm (Table 2a and 2b, Fig. 11a). 1631 rocks conform to the geochemical pattern of hypothetical basanitic parental magma (PA28) but have a slightly higher LILE/HFSE ratio as expected from evolved daughter rocks (Fig. 11a). Total REEs average 286 ppm in 1631 leucite phonolite, 282 ppm in leucite tephritic phonolite and 270 ppm in leucite phonolitic tephrite. The average LREE/HREE ratio is 45 in 1631 phonolite and 1631 tephritic phonolite and 43 in 1631 phono tephrite, as expected in rocks evolved from each other. In addition, a crossover occurs at Nd level, indicating that phonolites are enriched in LREE and notably in La.

The compositional ranges for the three 1631 rock-types substantially overlap with average orogenic Mediterranean basanites (Fig. 11b). There is a slightly negative Eu anomaly in the order of that observed in average Mediterrean basanites.

5.4 Petrogenesis

Both in middle ages and in modern times, Vesuvius issued olivine-bearing lavas during intra-Plinian activity by vents aligned WSW–ENE on the southern flank of the volcano [2, 17]. These Vesuvius phonolitic basanites (Table 2a and 2b) are here considered to have a primitive magmatic composition (*i.e.*, the Vesuvius parental melts). These lavas have modal olivine ~10%, MgO content > 7 wt.%, high $Mg_{\#}$ (83–86) and high Cr + Ni (usually in the 200–270 ppm range), which are very reasonable figures for primitive, mantle-derived melts [30]. CaO content is up to 12.9%, which is relatively high for alkaline basalts that usually have between 6 and 12%, but more similar to average Mediterranean basanites, which have 11.43 wt.% (Tab. 2a). Italian kamafugitic rocks contain much higher CaO (up to 15.4) but are intrinsically related to a carbonatitic component, which is not present at Vesuvius [31].

If we look at 'immobile couples' Hf/Zr and Ta/Nb ratios of all the rocks considered are distributed in a narrow range of variation (Fig. 12) around an average composition of Hf/Zr ratio of 0.023 and Ta/Nb ratio of 0.061, comprising 193 anorogenic Mediterranean samples which classify consistently as basanite [32]. Genuine basanites are rare in Italy and restricted to the Veneto Province [33] and Hyblean plateau [34]. In addition, there are some samples from the Roman Region [35]. Vesuvius basanitic lava PA28 and average historical Vesuvius lavas plot in the high Hf/Zr and low Ta/Nb quadrant with respect to average Mediterranean basanites and are more similar to Hyblean Distric and Roman Region basanites; whereas, Veneto district basanites have much higher Ta/Nb and thus represent a different mantle source (Fig. 12). Notably, average 1631 phonolitic tephrite is also very close to the average mediterrean basanites (Table 2a and 2b), suggesting a similar genetic condition.

The use of fractional crystallisation and mass balance modelling by petrologic software requires pressure (P) and temperature (T) inputs, which have to be obtained via mineralogical and geological constraints. Clinopyroxene, olivine ± Cr-spinel are the first phase to crystallise in primitive Vesuvius liquids [36] plus leucite at pressures > 2.5 kbar. The Fo content of olivine is used to estimate the crystallising melt temperature [37]. Olivines from 1631 samples average Fo_{96} and typically contain Cr_2O_3 + NiO between 0.01 and 0.03 wt.% (Table 3b); this could be a reaction product found in the skarns. Olivine from Vesuvius lavas have Fo content up to 90 mol.% [38]. According to correlation curves, Fo_{90} crystallising melt would have a maximum potential temperature of 1300°C [39]. This is in accordance with the liquidus T at 6 kbar modelled by software at 1280°C and is lower with respect to Italian primitive kamafugites, which are associated with carbonatites [40]. Mineralogy of 1631 deposits suggests that evolved 1631 magma rested in a magma chamber where low-pressure phases, such as leucite and vesuvianite can crystallise (max 2.5 kbar) [41, 42]. Coexistence of K-feldspar and leucite in the 1631 deposits constrains the temperature of the magma chamber at ~1090°C, based on the classical experimental phase equilibria results of [43] for the system NaAlSi3O8-KAlSi3O8-H2O. Recently, a pre-eruption temperature of 977 ± 30°C was computed for the 1631 eruption by [44] using the CaO content of the most felsic groundmass glass and CaO geothermometry. The minimum temperature of the 1631 magma crystallising inside the magma chamber is assumed to range from 1170 to 850°C based on homogenising temperatures of melt inclusions [45]. Leucite may be metastable during K-feld cristallisation, in this case a temperature between 900 and 850°C is reasonable at a late stage of melt evolution. These temperatures are also in agreement with $\delta^{34}S$ and Sulphur contents measured in 1631 volcanics by [46]. This pre-eruption temperature corresponds to a water pressure of $\sim$ 1.25 kbar along the incongruent melting curve of K-feldspar [43], whereas the uncertainties regarding the temperature estimated by [44] converts to a pressure range of $\sim$ 0.8 to 2.6 kbar. At water contents larger than 1 wt.%, the phonolitic melts has a very low viscosity even at temperature < 850°C [47]. A low pressure superficial chamber located about 1.5 km beneath the volcano is consistent with the caldera-like collapse of the main Vesuvius cone that occurred in the aftermath of the Nuées Ardentes phase of the 1631 eruption [13] and is confirmed by the comparison of the nature and distribution of lithic clast populations within the 1631 deposits and the stratigraphic sequence beneath the volcano [48]. The intense seismicity that occurred from 19th November to 16th December restricted to the villages surrounding the volcano also fit with a very superficial source.

In addition to literature data, we focused on the identification of a parental magma, which should rely both on compositional and textural constraints of the 1631 and the Vesuvius rocks. Among the Vesuvius phono-basanitic lavas with Mg# $\cong$ 80, PA28 sample is a suitable candidate for determining the parental liquid of the 1631 eruption.

Table 4: Physical characteristics of 1631 juvenile composition. Settling velocity of clinopyroxene, olivine and apatite were calculated by Stoke's law. Additional physical properties were obtained as output of PELE software calculations (see supplementary material 2)

Rock sample	Temperature °C	Viscosity 1 kg/m-s	Density of melt kg/m^3	Particle size mm	Density of crystal g/cm^3	Crystal settling m/day
PA28	1220	0,348	2800	1	3,27 forsterite	63,6
6 kbar				1	3,40 diopside	81,2
				0,1	3,19 apatite	0,53
TILES(4)D	1140	0,556	2790	1	3,27 forsterite	40,7
6 kbar				1	3,40 diopside	51,7
				0,1	3,19 apatite	0,34
F67PS(6)	940	0,962	2670	1	2,47 leucite	−9,80
2.5 kbar				0,1	3,19 apatite	0,25
F67PS(5)	840	0,800	2530	1	2,47 leucite	−3,50
0.5 kbar				0,1	3,19 apatite	0,39

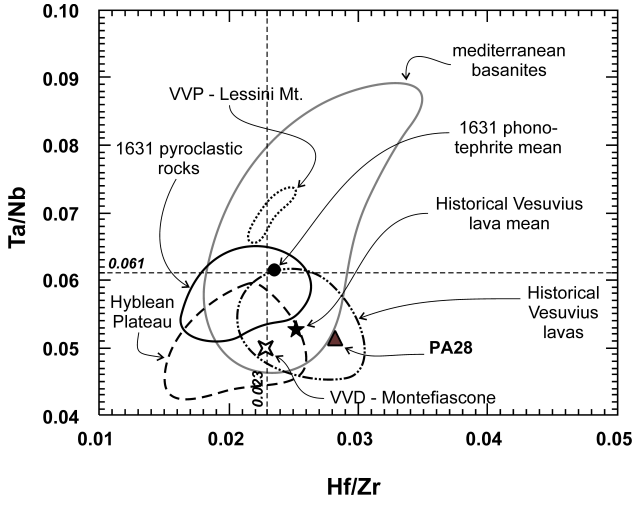

Figure 12: Ta/Nb vs. Hf/Zr diagram for 1631 Vesuvius rocks compared with anorogenic basanites from the Mediterranean Sea [32]. Dashed lines are average values for 193 Mediterranean basanites for which REE values are given in literature (http://georoc.mpch-mainz.gwdg.de/georoc). Plotting field of Vesuvius lavas overlaps with average Mediterrean basanites but have generally lower Ta/Nb and higher Hf/Zr, including Sample PA28. The 1631 rocks have lower Hf/Zr and more primitive samples of phonolitic tephrite composition are near average basanite values.

Starting from this composition, quantitative melt differentiation calculation was performed by mass balance and fractional crystallisation modelling using the Petrograph software [49] and equilibrium line of descent by the PELE software [50], assuming pressure between 6 and 0.5 kbar in accordance with field and mineralogical data. At higher pressure and lower quartz-magnetite-fayalite redox buffer (QMF) crystallisation models are invariably dominated by crystallisation of clinopyroxene, which appears early in the sequence, whereas olivine is subordinate (Fig. 13a, Supplementary materials 1). In fact, at lower pressures olivine crystallisation would be insufficient and plagioclase would disappear at equilibrium. Results of the crystal fractionation modelling suggest that at 6 kbar, Vesuvius phonolitic basanite can fractionate enough olivine (4.8%) and clinopyroxene (18%) to evolve to phono-thephritic composition (TILES) at ~1220°C with a QMF + 1. Plagioclase, nepheline and alkali feldspar crystallise in higher proportion and with lower olivine/plagioclase ratios in phono-tephritic composition (TILES) with respect to phonolitic basanite (PA28) at the same P and QMF but at a lower T < 1140°C (Fig. 13b). Such differentiation conditions are not possible at lower pressure and higher QMF. Further 3.6 wt.% olivine, plus 13.8 wt.% clinopyroxene and 1.3 wt.% of Ti-Magnetite fractionation would move the liquid to a tephritic phonolite (F67PS(6)) with a T decrease of ~90 °C, which virtually consumes all the olivine in the liquidus (Fig. 13c). Calculations indicate that the subsequent crystallising phases are invariably represented by leucite plus nepheline, clinopyroxene, magnetite, alkali feldspar and apatite, in excellent agreement with the mineral associations of the 1631 rocks. In the range of 1100–940°C, QMF +2 and 2.5 kbar, tephritic phonolite affected by crystal settling of 15.6 wt.% clinopyroxene, 8 wt.% leucite, 1.8 wt.% Ti-magnetite and 0.8 wt.% apatite would evolve to phonolite (Fig. 13d, Supplementary materials 2). At 0.5 kbar, modelling indicates that liquid becomes undersaturated in leucite at about 840°C and massive alkali feldspar crystallisation ~40 wt.% starts (Fig. 13d). The calculated liquid lines of descent fit well with the magmatic evolution from phonolitic basanite to phonolite, the latter representing the extreme differentiates at low T and P and high QMF. Therefore, modelling results indicate that "normative" passage from foidite to phonolite depends mainly on

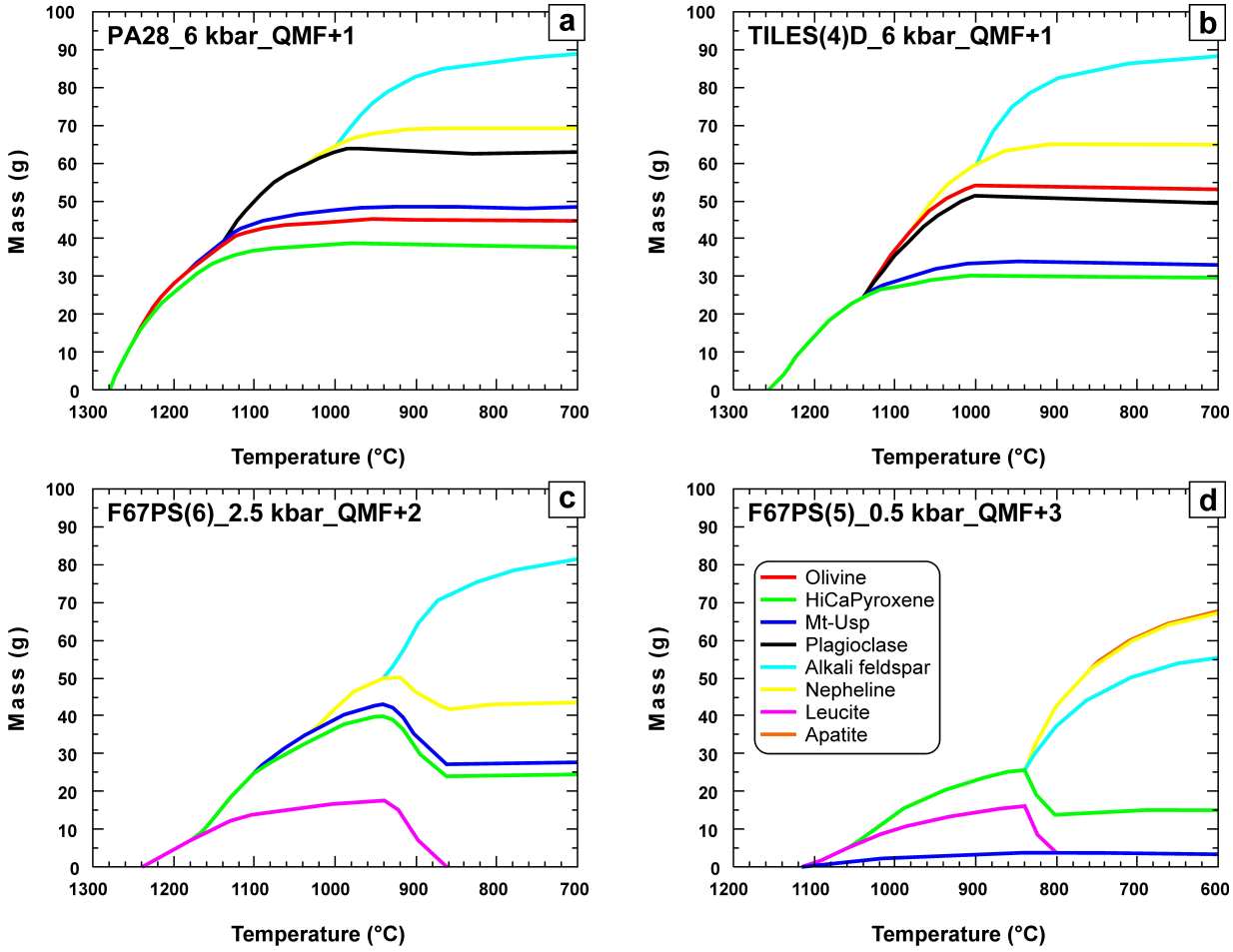

Figure 13: (a)–(d). Liquid line of descent for Vesuvius representing primitive phonolitic basanite and 1631 rock types (phonolitic tephrite, tephritic phonolite and phonolite), modelled by PELE software [50] at various pressures according to mineralogical and geological constraints (see supplementary material 1).

specific cpx, olivine crustal settling at a specific depth and temperature, that plagioclase and nepheline remain in the melt and that leucite may float from tephritic phonolite to phonolite (Table 4), where it may be unstable (Fig. 13d).

As a consequence, 1631 melt shows a sharp decrease of TiO_2, CaO, MgO, P_2O_5 and Cr + Ni during differentiation, a phenomenon well depicted by the $Ca_{\#}$/S.I. or $Mg_{\#}$/S.I. (Fig. 7e–7f). A negligible Eu anomaly (Fig. 11b) suggests that plagioclase did not contribute to the crystal settling.

Settling velocities of heavy minerals in such low-viscosity, volatile-rich melts is quite high and suggest a rapid melt differentiation (Table 4). Viscosity, volatile content and temperature was experimentally calculated for the 1631 phonolitic melt portion [47, 51, 52]. We calculated similar values for the main 1631 rock-types and crystal settling velocity using Stokes' law (Table 4). Different melt densities of calculated dense rock values suggest that in the magma chamber there were at least two liquids with different physical and chemical properties, which favoured relatively isolated, immiscible strata in the chamber. We speculate that the more primitive phonolitic tephrite was injected into the magma chamber at a time relatively close to the eruption. This explains why three different rock types were erupted at different times (phases) of the Plinian fallout, which represent a gradual magma chamber discharge from top to bottom.

As a whole, the liquid line of descent depicted in Figures 8, 9, 10 and 13 suggests that: (i) the parental 1631 magma (first appearing inside the magma chamber) is a phonolitic tephrite produced by olivine fractionation in a deep reservoir of a phonolitic basanite (similar to the most primitive Vesuvius erupted lavas and Hyblean and Roman Region basanites); (ii) the residual liquid evolved inside a crustal magma chamber to leucite tephritic phonolite and finally to leucite phonolite composition, at subsurface conditions.

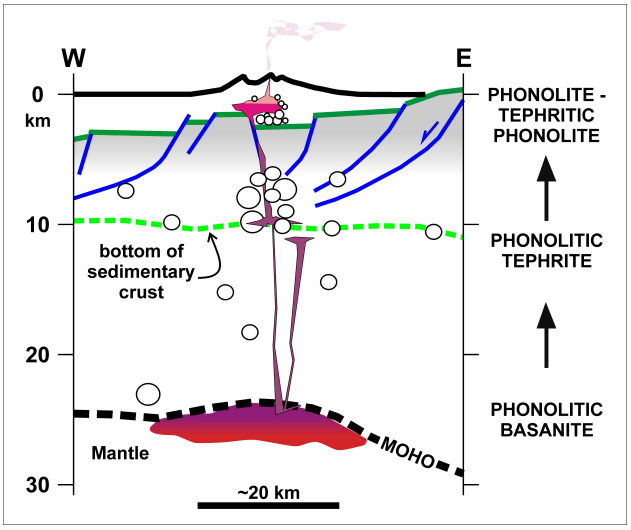

Figure 14: Idealised sketch of Vesuvius tectonic setting and various hypothetical levels of magma accumulation and differentiation. The sedimentary crust boundary, hypocentral foci and Moho are from [66, 68].

5.5 Carbon dioxide

Carbon dioxide in both 1631 apatites (see Section 3.3) and glass inclusion is negligible [44]. 1631 apatite composition are classified as mafic alkaline and are clearly different from those crystallising from CO_2-rich carbonate melts (Fig. 3d). At crustal pressure, the CO_2 production by melt/country rock reactions is likely limited to skarn formation. Geologic and textural evidence of a thin skarn shell in the 1631 eruption ejecta testify the small volume of *in situ* metasomatism and/or thermo-metamorphism at the magma chamber walls but do not imply *per se* substantial assimilation. Fresh sedimentary lithic clasts in the 1631 pyroclastic rocks are highly indicative of limited magma/crust interaction and thus potential assimilation. Skarn assemblages suggest temperatures of 650–700°C for the skarn forming processes, which typically include two types of metasomatic reactions, *i.e.*, formation of spinel-forsterite-calcite endoskarns by desilication of aluminosilicate bodies at the contact of dolostone wall rocks and reaction of pre-existing endoskarns with new influxes of magma and fluid as documented by [26, 27]. According to these authors, these metasomatic processes are promoted by CO_2-rich fluids and act as sinks of CO_2, producing calcite as part of the skarn mineral assemblage. It cannot be excluded that changes in temperature and CO_2 fugacity may drive these reactions in the opposite direction, destroying carbonate minerals and producing CO_2 [53]. The potential CO_2 produced is expected to escape towards the surface considering that: (i) the skarn shell prevents CO_2 movement from country rocks into the magma chamber and (ii) dissolution of CO_2 in the magma can be considered negligible at the relatively low pressure of the 1631 magma chamber (see above) based on the experimentally determined CO_2 solubility in melts (51).

The production of free CO_2 at deeper levels, through deep magma degassing or mantle degassing is very likely, considering the high flux of partly magmatic CO_2 discharged today in Central-Southern Italy, including the Vesuvian area [54, 55]. Nevertheless, the deeply originated CO_2 did not dissolve into the shallow 1631 magma chamber for the reasons noted above.

5.6 Limestone assimilation and AFC model

A substantial country-rock assimilation (>>10%) and consequent fractional crystallisation (AFC model) was assumed in the past literature at Vesuvius, originating from the classical work of [56]. This assumption was based on: (I) the widespread presence of limestones, dolostones and marls in the substratum of the volcano, (II) the presence of skarns as ejecta in the volcanics and (III) the abundant CO_2 emission at the surface. Assimilation of cold rocks on a large scale requires large amounts of heat and a proportionally larger amount of very hot magma. Felsic melts generated by underplating at the mantle crust boundary is likely but is a different assimilation model or better melting-mixing model [57–59]. Many authors strongly criticised this model being widely used for rocks similar to those of Vesuvius and raised objections based on thermodynamic grounds and geochemical evidences [60–62]. However, some authors, using an experimental approach, still assume that: (I) the Vesuvius primitive/parental melt is a trachy-basalt with MgO of $\sim$ 5 wt.% and temperature of $\sim$ 1100°C and (II) it assimilated significant amounts of limestone, thus chemically regressing to SiO_2-undersaturated tephritic compositions [7, 63]. This topic requires further discussion.

Geochemical features of the 1631 Vesuvius magma point to a mafic alkaline SiO_2-undersaturated parental melt, with a CaO content of 12.8 to 14.0 wt.%. Notionally, this composition may be obtained by desilication reactions driven by carbonate addition, such as:

$$CaAl_2Si_2O_8 + 2CaCO_3 = Ca_2Al(SiAl)O_7 + CaSiO_3 + 2CO_2 \quad (1)$$

$$NaAlSi_3O_8 + 2CaCO_3 = NaAlSiO_4 + 2CaSiO_3 + 2CO_2, \quad (2)$$

which may convert the basaltic assemblage (plagioclase dominated) into a nepheline-melilite bearing para-

genesis. In fact, these reactions form gehlenite and wollastonite, which are among the main constituents of melilite and diopside, respectively. The two main decarbonation reactions referred by [7] are either:

$$Mg_2SiO_4 + 3SiO_{2(melt)} + 2CaCO_3 = 2CaMgSi_2O_6 + 2CO_2, \quad (3)$$

if olivine is present, or:

$$MgO_{(melt)} + 2SiO_{2(melt)} + CaCO_3 = CaMgSi_2O_6 + CO_2, \quad (4)$$

if olivine is absent. Therefore, the main expected consequences of the progressive digestion of carbonates are destruction of forsteritic olivine, plagioclase and silica and production of CO_2 and diopsidic clinopyroxene.

It must be noted, however, that the experimental runs of [7] diverge on several aspects from the natural Vesuvius system and in particular from the 1631 magma chamber and related products. Therefore experimental results cannot be neatly applied to the 1631 case.

Secondly, in the TAS and de la Roche's diagrams, carbonate assimilation and related processes cause either a decrease in SiO_2 at constant $Na_2O + K_2O$ or a decrease in SiO_2 accompanied by an increase in $Na_2O + K_2O$ as recognised by [7] (see their Fig. 2 and related discussion). Both trends are roughly perpendicular to the 1631 evolution trend, as shown in Figure 9a and 9b, indicating that there is a marked contrast between the chemical changes driven by carbonate assimilation and the data from the 1631 natural system. The only common point between the experimental runs and the most primitive samples of the 1631 eruption is due to the artificial addition of olivine in the experiments.

6 Conclusions

6.1 Vesuvius parental melt

Although basanite modal compositions are not present among the 1631 samples, Vesuvius basanites exist, even if they were rarely reported in the Vesuvius literature, as already pointed out by [64]. We found that emission of basanitic lavas is characteristic of eccentric fissural eruptions that occurred during middle ages and also in modern times of Vesuvius activity (Table 2a and 2b, Fig. 9). From the modal point of view they are phonolitic tephrite (Ol < 10 vol.%) or phonolitic basanite (Ol ≥ 10 vol.%). From the chemical point of view (according to the diagram of [29], 1986, Fig. 9b) these rocks are confirmed to be basanites. Most primitive samples [*e.g.*, GV2 or Tiles(4)D in Table 2a and 2b] of the 1631 eruption are phonolitic tephrite but chemically they are close to basanitic composition, with MgO of 5.42 wt.%, $Mg_{\#}$ of 69 and Cr + Ni of 115 ppm. Normative calculation (CIPW of Fig. 10d) and the software-calculated liquid line of descent at equilibrium often indicates foidites at low pressure crystallisation; however, this is in contrast with essential plagioclase and k-feldspar in the modal composition of 1631 rocks.

6.2 Magma differentiation

The 1631 rocks (phonolite, tephritic phonolite and phonolitic tephrite) are likely produced by means of crystal fractionation processes in a primitive phono-basanitic melt, similar to that erupted during medieval and modern Vesuvius activity and having a composition similar to many other Mediterranean anorogenic basanites. Melt evolution developed through fractional crystallisation of olivine, clinopyroxene and plagioclase, plus nepheline and leucite at lower pressure and temperature. This evolution is reproducible by mass balance calculation and synthetic liquid line of descent with appropriate mineralogy. A first hypothesis is that the parental basanite melt might underplate at the base of the crust, at a depth of approximately 20 km [65]. We speculate that the primary basanite melt may have experienced an early stage of clinopyroxene and olivine separation and evolution to phonolitic tephrite evidenced by adcumulates (Fig. 13c) [39]. A further stage is upward migration and stationing in a crustal reservoir, possibly located ca. 8–9 km under Vesuvius [65] and coinciding with the base of the sedimentary cover (Fig. 14). At that pressure a reasonable temperature of 1190°C allows relatively moderate clinopyroxene and olivine fractionation and the melt to evolve significantly to thepritic phonolite (Fig. 13). Injection of tephritic phonolite melt into a subvolcanic magma chamber may have occurred through repeated refilling [14]. Crystallisation of K-feldspar and other minor phases may produce a layer of immiscible phonolitic liquids at pressures << 1 kbar and a T of about 840°C (Fig. 13). Leucite would be metastable in these conditions but its ability to float towards the top of the chamber explains melt undersaturation, which was previously interpreted as limestone assimilation and magma desilication. The observed and calculated crystallisation patter does not require assimilation; crystal fractionation is a sufficient condition. A further injection of hot phono-tephritic melt inside the 1631 magma chamber was likely favoured by local tectonic events accounted for by relatively intense volcano tectonic earthquakes felt in Naples during the five years prior to the eruption [16].

6.3 Magma chamber breakage and eruption scenario

At the wall-rock/magma interface of the magma chamber, represented by the skarn carapace, internal volatile-supported pressure closely balances the external (overburden) pressure as suggested by the relatively long-term magma differentiation without magma chamber deformation. This delicate equilibrium was probably destabilised by the last refilling of fresh magma from the deep reservoir producing sudden breakage of the country rocks accompanied by a notable number of local shakes in the two months before the 1631 eruption. This mechanism is consistent with the presence of both long- and short-term precursors before the 1631 eruption and distribution of recent instrumental ipocentral locations (Fig. 14) [66]. The inferred scenario for the next explosive eruption at Vesuvius involves the formation of a magma chamber, produced by the rising and stationing at shallow depth of a magma batch, possibly accompanied by volcano tectonic earthquakes felt over a large area. The melt in this chamber would stratify and crystallise rapidly, producing volatile pressures that might be able to trigger an explosive eruption in times that are essentially dependent on the frequency and volume of the subsequent feeding events. Vesuvius seismicity suggests two possible volcano seismogenetic levels similar to those hypothesised for the 1631 precursors; however, seismic activity is low and no sequences comparable to those of the 1616 to 1630 period have since occurred. A further scenario is possible, either in the absence of the magma chamber, or in its presence if the uprising phono-tephritic or phono-basanitic magma does not enter the chamber, of discharging directly to the surface through fractures dissecting the low flanks of the volcano. This is a comparatively less severe scenario but low-level vent locations and related outpouring lava would be locally disastrous on the very densely populated coastal band.

Acknowledgement: Massimo Guidi and Ilaria Baneschi (IGG-CNR) performed CO_2 bulk rock analyses. Frances Wall and EMMA staff at NHM is acknowledged for their kind assistance during apatite EMP analyses. Olivine analyses are courtesy of Geosciences Department of Padua University. We are grateful to Luigi Marini for the useful discussions on CO_2 role, and to Giada Iacono-Marziano for valuable suggestions about improvement of an earlier version of the manuscript.

References

[1] Arnò V., Principe C., Rosi M., Santacroce R., Sbrana A., Sheridan M.F., Eruptive history. In: Santacroce R. (Ed.), Somma-Vesuvius. CNR Edizioni, Roma, 1987, 114(8), 53-104

[2] Principe C., Tanguy J.C., Arrighi S., Paiotti A., Le Goff M., Zoppi U., Chronology of Vesuvius activity from A.D. 79 to 1631 based on archeomagnetism of lavas and historical sources. Bull. Volcanol., 2004, 66, 703-724

[3] Arrighi S., Principe C., Rosi M., Violent strombolian and subplinian eruption at Vesuvius during the post-1631 activity. Bull. Volcanol., 2001, 63, 126-150

[4] Ayuso R.A., De Vivo B., Rolandi G., Seal II R.R., Paone A., Geochemical and isotopic (Nd-Pb-Sr-O) variations bearing on the genesis of volcanic rocks from Vesuvius, Italy. J. Volcanol. Geotherm. Res., 1998, 82, 53-78

[5] Le Maitre R.W., Igneous Rocks: A Classification and Glossary of Terms, 2nd ed. Cambridge University Press, Cambridge, 2002

[6] Cioni R., Volatile content and degassing processes in the AD 79 magma chamber at Vesuvius (Italy). Contrib. Mineral. Petrol., 2000, 140, 40-54

[7] Iacono Marziano G., Gaillard F., Pichavant M., Limestone assimilation by basaltic magmas: an experimental re-assessment and application to Italian volcanoes. Contrib. Mineral. Petrol., 2008, 155, 719-738

[8] Civetta L., Galati R., Santacroce R., Magma mixing and convective compositional layering within the Vesuvius magma chamber. Bull. Volcanol., 1991, 53, 287-300

[9] Morgan D.J., Blake S., Rogers N.W., De Vivo B., Rolandi G., Davidson J.P., Magma chamber recharge at Vesuvius in the century prior to the eruption of A.D. 79. Geology, 2006, 34 (10), 845-848

[10] Degruyter W., Huber C., A model for eruption frequency of upper crustal silicic magma chambers. Earth Planet. Sci. Lett., 2014, 403, 117-130

[11] Barberi F., Davis M.S., Isaia R., Nave R., Ricci T., Volcanic risk perception in the Vesuvius population. J. Volcanol. Geotherm. Res., 2008, 172(3-4), 244-258

[12] Heiken G., Will Vesuvius erupt? Three million people need to know. Science, 1999, 286, 1685-1687

[13] Rosi M., Principe C., Vecci R., The 1631 Vesuvius eruption. A reconstruction based on historical and stratigraphical data. J. Volcanol. Geotherm. Res., 1993, 58, 151-182

[14] Principe C., Marini L., Evolution of the Vesuvius magmatic-hydrothermal system before the 16 December 1631 eruption. J. Volcanol. Geotherm. Res., 2008, 171, 301-306

[15] Principe C., The 1631 eruption of Vesuvius: Volcanological concepts in Italy at the beginning of the XVII century. In: Morello N. (Ed.), Volcanoes and History. Proceedings of the 20th INHIGEO Symposium, Naples, Aeolian Islands, Catania, September 19-25 1995, 525-54, Brigatti Editore, Genova, 1998

[16] Guidoboni E., Mariotti D., Vesuvius: Earthquakes from 1600 up to the 1631 eruption. J. Volcanol. Geotherm. Res., 2011, 200(4), 267-272

[17] Paolillo A., Principe C., Bisson M., Gianardi R., Giordano D., La Felice S., Volcanology of the South-Western sector of Vesuvius, Italy. J. Maps, 2016, 12, 425-440, DOI 10.1080/17445647.2016.1234982

[18] Stormer J.C., Pierson M.L., Tacker R.C., Variation of F and Cl X-ray intensity due to anisotropic diffusion in apatite during electron microprobe analysis. Am. Mineral., 1993, 78, 641-648
[19] Greenwood J.P., Itoh S., Sakamoto N., Warren P., Taylor L., Yurimoto H., Hydrogen isotope ratios in lunar rocks indicate delivery of cometary water to the Moon. Nat. Geosci., 2011, 4, 79-82
[20] McCubbin F.M., Steele A., Hauri E.H., Nekvasil H., Yamashita S., Hemley R.J., Nominally hydrous magmatism on the Moon. Proc. Natl. Acad. Sci. U. S. A., 2010, 107(25), 11223-11228
[21] Piccoli P., Candela P., Apatite in felsic rocks: a model for the estimation of initial halogen concentration in the Bishop Tuff (Long Valley), and Tuolumne intrusive suite (Sierra Nevada Batholith) magmas. Am. J. Sci., 1994, 294, 92-135
[22] Liu Y., Stoppa F., Tonucci L., Mingsheng P., Study on ^{1}H NMR Spectroscopy of Fluor-hydroxylapatite. J. Chin. Ceram. Soc., 2002, 30, 42-44.
[23] Liu Y., Comodi P., Sassi P., Vibrational spectroscopic investigation of phosphate tetrahedron in fluor-, hydroxy-, and chlorapatites. N. Jb. Miner. Abh., 1998, 174(2), 211-222, doi:10.1127/njma/174/1998/211
[24] Comodi P., Liu Y., Stoppa F., Woolley A.R., A multi-method analysis of Si-, S- and REE-rich apatite from a new find of kalsilite-bearing leucitite (Abruzzi, Italy). Mineral. Mag., 1999, 63(5), 661-672
[25] Stoppa F., Liu Y., Chemical composition and petrogenetic implications of apatites from some ultra-alkaline Italian rocks. Eur. J. Mineral., 1995, 7, 391-402
[26] Pascal M.-.L, Di Muro A., Fonteilles M., Principe C., Zirconolite and calzirtite in banded forsterite-spinel-calcite skarn ejecta from the 1631 eruption of Vesuvius: inferences for magma-wallrock interactions. Mineral. Mag., 2009, 73(2), 333-356
[27] Pascal M.-L., Fonteilles M., Boudouma O., Principe C., Qandilite from Vesuvius skarn ejecta: conditions of formation and miscibility gap in the ternary Spinel-Qandalite-Magnesioferrite. Can. Mineral., 2011, 49(2), 459-485
[28] Kuno H., Yamasaki K., Iida C., Nagashima K., Differentiation of Hawaii magmas. Jpn. J. Geol. Geogr., 1957, 28, 179-218
[29] de La Roche H., Classification et nomenclature des roches ignées: un essai de restauration de la convergence entre systématique quantitative, typologie d'usage et modélisation génétique. Bull. Soc. Geol. Fr., 1986, 2, 337-353
[30] Wilson B.M., Igneous petrogenesis a global tectonic approach. Spinger, 2007
[31] Stoppa F., Schiazza M., An overview of monogenetic carbonatitic magmatism from Uganda, Italy, China and Spain: Volcanological and geochemical features. J. South Am. Earth Sci., 2013, 41, 140-159
[32] Lustrino M., Wilson M., The circum-Mediterranean anorogenic Cenozoic igneous province. Earth-Sci. Rev., 2007, 81, 1-65
[33] Gasperini D., Bosch D., Braga R., Bondi M., Macera P., Morten L., Ultramafic xenoliths from the Veneto Volcanic Province (Italy): Petrological and geochemical evidence for multiple metasomatism of the SE Alps mantle lithosphere. Geochem. J., 2006, 40, 377-404
[34] Bianchini G., Clocchiatti R., Coltorti M., Joron J.L., Vaccaro C., Petrogenesis of mafic lavas from the northernmost sector of the Iblean District (Sicily). Eur. J. Mineral., 1998, 10, 301-315
[35] Gasperini D., Blichert-Toft J., Bosch D., Del Moro A., Macera P., Albarede F., Upwelling of deep mantle material through a plate window: evidence from the geochemistry of Italian basaltic volcanics. J. Geophys. Res., 2002, 47, 30-38
[36] Pichavant M., Scaillet B., Pommier A., Iacono-Marziano G., Cioni R., Nature and evolution of primitive Vesuvius magmas: An experimental study. J. Petrol., 2014, 55(11), 2281-2310
[37] Beattie P.D., Ford C.E., Russell D.G., Partition coefficients for olivine-melt and orthopyroxene-melt systems. Contrib. Mineral. Petrol., 1991, 109(2), 212-224
[38] Cigolini C., Thermobarometry of phlogopite-bearing dunitic enclaves from Mount Vesuvius: preliminary estimates. Atti R. Accad. Sci. Torino, Cl. Sci. Fis., Mat. Nat., 1997, 131, 33-56
[39] Nisbet E.G., Cheadle M.J., Arndt N.T., Bickle M.J., Constraining the potential temperature of the Archaean mantle: A review of the evidence from komatiites. Lithos, 1993, 30, 291-307
[40] Cundari A., Ferguson A.J., Petrogenetic relationships between melilitite and lamproite in the Roman Comagmatic Region: the lavas of S. Venanzo and Cupaello. Contrib. Mineral. Petrol., 1991, 107(3), 343-357
[41] Normand C., Williams-Jones A.E., Physicochemical conditions and timing of rodingite formation: evidence from rodingite-hosted fluid inclusions in the JM Asbestos mine, Asbestos, Québec. Geochem. Trans., 2007, 8, doi:10.1186/1467-4866-8-11
[42] Liu L.-G., High pressure phase transitions of potassium aluminosilicates with emphasis on leucite. Contrib. Mineral. Petrol., 1987, 95, 1-3
[43] Ehlers E.G., The interpretation of geological phase diagrams. Freeman, W.H., & Co, San Francisco, 1972
[44] Scaillet B., Pichavant M., Cioni R., Upward migration of Vesuvius magma chamber over the past 20,000 years. Nature, 2008, 455, 216-220
[45] Cortini M.A., Lima A., Devivo B., Trapping temperatures of melt inclusions from ejected Vesuvian mafic xenoliths. J. Volcanol. Geotherm. Res., 1985, 26, 167-172
[46] Marini L., Chiappini V., Cioni R., Cortecci G., Dinelli E., Principe C., Ferrara G., Effect of degassing on sulfur contents and δ^{34}S values in Somma-Vesuvius magmas. Bull. Volcanol., 1998, 60(3), 187-194
[47] Romano C., Giordano D., Papale P., Mincione V., Dingwell D.B., Rosi M., The dry and hydrous viscosities of alkaline melts from Vesuvius and Phlegrean Fields. Chem. Geol., 2003, 202(1-2), 23-38
[48] Brocchini D., Principe C., Castradori D., Laurenzi M.A., Gorla L., Quaternary evolution of the southern sector of the Campanian Plain and early Somma-Vesuvius activity: insights from the Trecase 1 well. Mineral. Petrol., 2001, 73, 67-91
[49] Petrelli M., Poli G., Perugini D., Peccerillo A., Petrograph: a New Software to Visualize, Model, and Present Geochemical Data in Igneous Petrology. Geochem. Geophys. Geosyst., 2005, 6, Q07011, doi: 10.1029/2005GC000932
[50] Boudreau A.E., PELE - a version of the MELTS software program for the PC platform. Comput. Geosci., 1999, 25, 201-203, https://nicholas.duke.edu/people/faculty/boudreau/DownLoads.html
[51] Carroll M.R., Blank J.G., The solubility of H_2O in phonolitic melts. Am. Mineral., 1997, 82, 549-556
[52] Chiodini G., Marini L., Russo M., Geochemical evidence for the existence of high-temperature hydrothermal brines at Vesuvio volcano, Italy. Geochim. Cosmochim. Acta, 2001, 65, 2129-2147
[53] Holloway J.R., Blank J.G., Application of experimental results to C-O-H species in natural melts. Rev. Mineral. Geochem., 1994,

30, 187-230

[54] Gambardella B., Cardellini C., Chiodini G., Frondini F., Marini L., Ottonello G., Vetuschi Zoccolini M., Fluxes of deep CO_2 in the volcanic areas of central-southern Italy. J. Volcanol. Geotherm. Res., 2004, 136, 31-52

[55] Rogie J.D., Kerrick D.M., Chiodini G., Frondini F., Flux measurements of non volcanic CO_2 emission from some vents in central Italy. J. Geophys. Res., 2000, 105(B4), 8435-8445

[56] Rittmann A., Die geologisch bedingte Evolution und Differentiation des Somma-Vesuv magmas. Zeit. Vulkan., 1933, 15(1/2), 8-94

[57] Lavecchia G., Stoppa, F., The tectonic significance of Italian magmatism: an alternative view to the popular interpretation. Terra Nova, 1996, 8, 435-446

[58] Wiesmaier S., Trol V.R., Carracedo J.C., Ellam R.M., Bindeman I., Wolff J.A., Bimodality of lavas in the Teide-Pico Viejo succession in Tenerife: The role of crustal melting in the origin of recent phonolites. J. Petrol., 2012, 53, 2465-2495

[59] Watkinson D.H., Wyllie P.J., Phase equilibrium studies bearing on the limestone assimilation hypothesis. Geol. Soc. Am. Bull., 1969, 80(8), 1565-1576

[60] Bailey D.K., Carbonate volcanics in Italy: numerical tests for the hypothesis of lava-sedimentary limestone mixing. Period. Mineral., 2005, 74(3), 205-208

[61] Bell K., Kjarsgaard B., Discussion of Peccerillo (2004) "Carbonate-rich pyroclastic rocks from Central Apennines: carbonatites or carbonate-rich rocks? Period. Mineral., 2006, 75(1), 85-92

[62] Woolley R.A., Bailey D.K., Castorina F., Rosatelli G., Stoppa F., Wall F., Reply to: "Carbonate-rich pyroclastic rocks from central Apennines: carbonatites or carbonated rocks? A commentary". A. Peccerillo. Period. Mineral., 2005, 74(3), 183-194

[63] Iacono Marziano G., Gaillard F., Scaillet B., Pichavant M., Chiodini G., Role of non-mantle CO_2 in the dynamics of volcano degassing: The Mount Vesuvius example. Geology, 2009, 37, 319-322, doi: 10.1130/G25446A.1

[64] Cigolini C., Petrography and thermobarometry of high-pressure ultramafic ejecta from Mount Vesuvius, Italy: inferences on the deep feeding system. Period. Mineral., 2007, 76(2-3), 5-24

[65] Milia A., Torrente M.M., The possible role of extensional faults in localizing magmatic activity: a crustal model for the Campanian Volcanic Zone (eastern Tyrrhenian Sea, Italy). J. Geol. Soc. (London, U.K.), 2011, 168, 471-484

[66] Chiarabba C., Jovane L., DiStefano R., A new view of Italian seismicity using 20 years of instrumental recordings. Tectonophysics, 2005, 395, 251-268

[67] Sun S., McDonought W.F., Chemical and isotopic systematic in ocean basalt: implication for mantle composition and processes. In: Saunders A.D., Norry M.J. (Eds.), Magmatism in the Ocean Basins, Geological Society, 1989, 42, 313-345

[68] Cassinis R., Scarascia S., Lozej A., The deep crustal structure of Italy and surrounding areas from seismic refraction data; a new synthesis. Boll. Soc. Geol. Ital., 2003, 122 (3), 365-376

Supplementary Material 1

PA28_1300-700 °C_6000 bar_Ol, Cpx, Plg, K-feld, Mt-Usp, Ne, Ap_QMF+1_EQUILIBRIUM

Step: 31 CONSTRAINTS: Equilibrium ISOBARIC O2 buffer: QFM+1
Log f(O2): Not determined Log f(S2): Not determined
TEMPERATURE: 700.00°C PRESSURE: 6000.00 bars
BULK: MASS: 100.18 g V: 33.81 cm3 DENSITY: 2.96 g/cm3 EFF. VISCOSITY: 35.63 log(poise)
G: -14768.37 J/g H: -12916.94 J/g S: 1.897 J/K-g Cp: 1.17 J/K-g

LIQUID: MASS: 11.67 g V: 4.21 cm3 DENSITY: 2.77 g/cm3 VISCOSITY: 18.14 log(poise) Giordano et al. (2007)
LPSI
G: -14485.53 J/g H: -12568.30 J/g S: 1.97 J/K-g Cp: 1.50 J/K-g
LIQUID COMPOSITION (wt%):

SiO2	TiO2	Al2O3	Fe2O3	Cr2O3	FeO	MnO	MgO	CaO	Na2O	K2O	P2O5	H2O	CO2	S
33.582	6.529	25.139	0.002	0.000	0.043	1.140	0.085	8.154	0.016	18.645	6.665	0.000	0.000	0.000

SATURATED PHASES:
BULK MASS: 88.51 g BULK VOLUME: 29.59 cm3 BULK DENSITY: 2.99 g/cm3

PHASE	AFFINITY	MASS	TOTAL MASS	COMPOSITION			
HiCaPyroxene	0.02	37.651	37.65	di	:0.8079	hd	:0.1921
Olivine	0.00	6.992	6.99	fo	:0.6710	fa	:0.3290
Mt-Usp	3.89	3.383	3.38	mt	:0.4950	usp	:0.5050
Plagioclase	0.04	14.129	14.13	an	:0.9419	ab	:0.0581
Nephaline(pure)	0.16	6.854	6.85	ne	:1.0000		
AlkaliFeldspar	0.04	19.502	19.50	or	:1.0000		

UNDERSATURATED PARTICIPATING MINERALS:

PHASE	AFFINITY	COMPOSITION

TILES(4)D_1300-700 °C_6000 bar_Ol, Cpx, Plg, K-feld, Mt-Usp, Ne, Ap_QMF+1_EQUILIBRIUM

Step: 31 CONSTRAINTS: Equilibrium ISOBARIC O2 buffer: QFM+1
Log f(O2): Not determined Log f(S2): Not determined
TEMPERATURE: 700.00°C PRESSURE: 6000.00 bars
BULK: MASS: 100.20 g V: 34.81 cm3 DENSITY: 2.88 g/cm3 EFF. VISCOSITY: 34.97 log(poise)
G: -14870.32 J/g H: -12994.14 J/g S: 1.921 J/K-g Cp: 1.18 J/K-g

LIQUID: MASS: 12.00 g V: 4.37 cm3 DENSITY: 2.75 g/cm3 VISCOSITY: 17.47 log(poise) Giordano et al. (2007)
LPSI
G: -14529.84 J/g H: -12611.60 J/g S: 1.97 J/K-g Cp: 1.50 J/K-g
LIQUID COMPOSITION (wt%):

SiO2	TiO2	Al2O3	Fe2O3	Cr2O3	FeO	MnO	MgO	CaO	Na2O	K2O	P2O5	H2O	CO2	S
34.724	5.285	25.514	0.002	0.000	0.047	1.095	0.079	7.928	0.021	18.821	6.484	0.000	0.000	0.000

SATURATED PHASES:
BULK MASS: 88.19 g BULK VOLUME: 30.44 cm3 BULK DENSITY: 2.90 g/cm3

PHASE	AFFINITY	MASS	TOTAL MASS	COMPOSITION			
HiCaPyroxene	0.02	29.559	29.56	di	:0.7942	hd	:0.2058
Mt-Usp	6.68	3.565	3.56	mt	:0.5205	usp	:0.4795
Plagioclase	0.02	16.208	16.21	an	:0.9440	ab	:0.0560
Olivine	0.00	3.618	3.62	fo	:0.6245	fa	:0.3755
Nephaline(pure)	0.11	11.856	11.86	ne	:1.0000		
AlkaliFeldspar	0.02	23.386	23.39	or	:1.0000		

UNDERSATURATED PARTICIPATING MINERALS:

PHASE	AFFINITY	COMPOSITION

F67PS(6)_1300-700 °C_2500 bar_ Cpx, K-feld, Mt-Usp, Ne, Lc, Ap_QMF+2_EQUILIBRIUM

Step: 31 CONSTRAINTS: Equilibrium ISOBARIC O2 buffer: QFM+2 MASS O2 ADDED: -0.00042 g
Log f(O2): -11.61 (Kress and Carmichael model) Log f(S2): Not determined
TEMPERATURE: 700.00°C PRESSURE: 2500.00 bars
BULK: MASS: 100.22 g V: 36.04 cm3 DENSITY: 2.78 g/cm3 EFF. VISCOSITY: 35.93 log(poise)
G: -15044.46 J/g H: -13139.42 J/g S: 1.953 J/K-g Cp: 1.22 J/K-g

LIQUID: MASS: 18.97 g V: 6.99 cm3 DENSITY: 2.72 g/cm3 VISCOSITY: 18.44 log(poise) Giordano et al. (2007)
LPSI
G: -15689.24 J/g H: -13748.90 J/g S: 1.99 J/K-g Cp: 1.58 J/K-g
LIQUID COMPOSITION (wt%):

SiO2	TiO2	Al2O3	Fe2O3	Cr2O3	FeO	MnO	MgO	CaO	Na2O	K2O	P2O5	H2O	CO2	S
39.993	3.410	34.434	0.251	0.000	0.066	0.695	0.031	13.520	0.587	4.661	2.352	0.000	0.000	0.000

SATURATED PHASES:
BULK MASS: 81.24 g BULK VOLUME: 29.06 cm3 BULK DENSITY: 2.80 g/cm3

PHASE	AFFINITY	MASS	TOTAL MASS	COMPOSITION			
HiCaPyroxene	0.01	24.185	24.19	di	:0.6743	hd	:0.3257
Mt-Usp	0.02	3.223	3.22	mt	:0.9310	usp	:0.0690
Nephaline(pure)	0.00	16.221	16.22	ne	:1.0000		
AlkaliFeldspar	0.00	37.615	37.61	or	:1.0000		

UNDERSATURATED PARTICIPATING MINERALS:

PHASE	AFFINITY	COMPOSITION
Leucite (pure)	4452.77	Pure phase

F67PS(5)_1200-600 °C_500 bar_ Cpx, K-feld, Mt-Usp, Ne, Lc, Ap_QMF+3_EQUILIBRIUM

Step: 31 CONSTRAINTS: Equilibrium ISOBARIC O2 buffer: QFM+3 MASS O2 ADDED: -0.00232 g
Log f(O2): Not determined Log f(S2): Not determined
TEMPERATURE: 600.00°C PRESSURE: 500.00 bars
BULK: MASS: 100.22 g V: 38.17 cm3 DENSITY: 2.63 g/cm3 EFF. VISCOSITY: 14.66 log(poise)
G: -15112.73 J/g H: -13426.04 J/g S: 1.937 J/K-g Cp: 1.28 J/K-g

LIQUID: MASS: 32.51 g V: 13.30 cm3 DENSITY: 2.44 g/cm3 VISCOSITY: 12.36 log(poise) Giordano et al. (2007)
LPSI
G: -15863.82 J/g H: -13993.34 J/g S: 2.16 J/K-g Cp: 1.62 J/K-g
LIQUID COMPOSITION (wt%):

SiO2	TiO2	Al2O3	Fe2O3	Cr2O3	FeO	MnO	MgO	CaO	Na2O	K2O	P2O5	H2O	CO2	S
49.003	1.281	26.617	0.716	0.000	0.013	0.401	0.003	9.939	5.446	2.389	0.709	3.484	0.000	0.000

SATURATED PHASES:
BULK MASS: 67.71 g BULK VOLUME: 24.86 cm3 BULK DENSITY: 2.72 g/cm3

PHASE	AFFINITY	MASS	TOTAL MASS	COMPOSITION			
Mt-Usp	0.02	3.122	3.12	mt	:0.8845	usp	:0.1155
HiCaPyroxene	0.07	12.099	12.10	di	:0.6047	hd	:0.3953
AlkaliFeldspar	0.00	40.250	40.25	or	:1.0000		
Nephaline(pure)	0.00	12.239	12.24	ne	:1.0000		

UNDERSATURATED PARTICIPATING MINERALS:

PHASE	AFFINITY	COMPOSITION
Leucite (pure)	7879.81	Pure phase
Apatite	363.71	Pure phase

Supplementary Material 2

PA28_6 kbar_QMF+1

```
Step: 5  CONSTRAINTS: Equilibrium  ISOBARIC   O2 buffer: QFM+1  MASS O2 ADDED: -0.01066 g
Log f(O2): -6.66 (Kress and Carmichael model)   Log f(S2): Not determined
TEMPERATURE: 1220.00°C   PRESSURE: 6000.00 bars
BULK:     MASS: 100.15 g   V: 35.72 cm3   DENSITY: 2.80 g/cm3   EFF. VISCOSITY: 3.48 log(poise)
             G: -15920.19 J/g   H: -12028.63 J/g   S: 2.606 J/K-g    Cp: 1.42 J/K-g

LIQUID:   MASS: 76.91 g   V: 28.46 cm3   DENSITY: 2.70 g/cm3   VISCOSITY: 3.13 log(poise) Giordano et al. (2007) LPSI
             G: -15826.69 J/g   H: -11806.06 J/g   S: 2.69 J/K-g    Cp: 1.49 J/K-g
      LIQUID COMPOSITION (wt%):
      SiO2  TiO2  Al2O3 Fe2O3 Cr2O3 FeO   MnO   MgO   CaO   Na2O  K2O   P2O5  H2O   CO2   S
      47.1511.331 18.2211.988 0.000 6.006 0.173 5.052 9.882 2.063 7.121 1.012 0.000 0.000 0.000

SATURATED PHASES:
         BULK MASS: 23.24 g   BULK VOLUME: 7.26 cm3   BULK DENSITY: 3.20 g/cm3
      PHASE            AFFINITY    MASS  TOTAL MASS  COMPOSITION
      HiCaPyroxene       0.00    21.793     21.79    di   :0.8628  hd   :0.1372
      Olivine            0.00     1.451      1.45    fo   :0.8277  fa   :0.1723

UNDERSATURATED PARTICIPATING MINERALS:
      PHASE            AFFINITY        COMPOSITION
      Plagioclase       7231.17  an   :0.8256  ab   :0.1744
      AlkaliFeldspar   10959.76  Pure phase
      Mt-Usp            7867.44  mt   :0.9483  usp  :0.0517
      Nephaline(pure)  11674.30  Pure phase
```

TILES(4)D_6 kbar_QMF+1

```
Step: 10  CONSTRAINTS: Equilibrium  ISOBARIC   O2 buffer: QFM+1  MASS O2 ADDED: -0.00292 g
Log f(O2): -8.62 (Kress and Carmichael model)   Log f(S2): Not determined
TEMPERATURE: 1120.00°C   PRESSURE: 6000.00 bars
BULK:     MASS: 100.12 g   V: 35.83 cm3   DENSITY: 2.79 g/cm3   EFF. VISCOSITY: 5.56 log(poise)
             G: -15783.73 J/g   H: -12305.08 J/g   S: 2.497 J/K-g    Cp: 1.43 J/K-g

LIQUID:   MASS: 69.32 g   V: 26.18 cm3   DENSITY: 2.65 g/cm3   VISCOSITY: 5.07 log(poise) Giordano et al. (2007) LPSI
             G: -15793.00 J/g   H: -12153.90 J/g   S: 2.61 J/K-g    Cp: 1.54 J/K-g
      LIQUID COMPOSITION (wt%):
      SiO2  TiO2  Al2O3 Fe2O3 Cr2O3 FeO   MnO   MgO   CaO   Na2O  K2O   P2O5  H2O   CO2   S
      47.3221.254 23.5821.116 0.000 4.492 0.190 1.996 6.178 3.779 8.968 1.123 0.000 0.000 0.000

SATURATED PHASES:
         BULK MASS: 30.80 g   BULK VOLUME: 9.65 cm3   BULK DENSITY: 3.19 g/cm3
      PHASE            AFFINITY    MASS  TOTAL MASS  COMPOSITION
      HiCaPyroxene       0.00    26.518     26.52    di   :0.8139  hd   :0.1861
      Mt-Usp             0.00     0.653      0.65    mt   :0.9147  usp  :0.0853
      Plagioclase        0.00     3.136      3.14    an   :0.8041  ab   :0.1959
      Olivine            0.00     0.491      0.49    fo   :0.7406  fa   :0.2594

UNDERSATURATED PARTICIPATING MINERALS:
      PHASE            AFFINITY        COMPOSITION
      AlkaliFeldspar    7576.59  Pure phase
      Nephaline(pure)   2872.71  Pure phase
```

F67PS(6)_2.5 kbar_QMF+2

```
Step: 19  CONSTRAINTS: Equilibrium  ISOBARIC   O2 buffer: QFM+2  MASS O2 ADDED: -0.00032 g
Log f(O2): -9.54 (Kress and Carmichael model)   Log f(S2): Not determined
TEMPERATURE: 940.00°C   PRESSURE: 2500.00 bars
BULK:     MASS: 100.22 g   V: 37.60 cm3   DENSITY: 2.67 g/cm3   EFF. VISCOSITY: 9.62 log(poise)
             G: -15550.84 J/g   H: -12759.28 J/g   S: 2.301 J/K-g    Cp: 1.35 J/K-g

LIQUID:   MASS: 50.20 g   V: 19.87 cm3   DENSITY: 2.53 g/cm3   VISCOSITY: 8.52 log(poise) Giordano et al. (2007) LPSI
             G: -16102.53 J/g   H: -13193.76 J/g   S: 2.40 J/K-g    Cp: 1.57 J/K-g
      LIQUID COMPOSITION (wt%):
      SiO2  TiO2  Al2O3 Fe2O3 Cr2O3 FeO   MnO   MgO   CaO   Na2O  K2O   P2O5  H2O   CO2   S
      53.9741.201 25.0320.587 0.000 0.771 0.263 0.187 6.083 4.209 6.804 0.889 0.000 0.000 0.000

SATURATED PHASES:
         BULK MASS: 50.03 g   BULK VOLUME: 17.72 cm3   BULK DENSITY: 2.82 g/cm3
      PHASE            AFFINITY    MASS  TOTAL MASS  COMPOSITION
      Leucite (pure)     0.00    17.767     17.77    le   :1.0000
      HiCaPyroxene       0.00    22.092     22.09    di   :0.7160  hd   :0.2840
      Mt-Usp             0.00     3.125      3.12    mt   :0.9000  usp  :0.1000
      Nephaline(pure)    0.00     7.046      7.05    ne   :1.0000

UNDERSATURATED PARTICIPATING MINERALS:
      PHASE            AFFINITY        COMPOSITION
      AlkaliFeldspar     670.93  Pure phase
```

F67PS(5)_0.5 kbar_QMF+3

Step: 20 CONSTRAINTS: Equilibrium ISOBARIC O2 buffer: QFM+3 MASS O2 ADDED: -0.00484 g
Log f(O2): -10.25 (Kress and Carmichael model) Log f(S2): Not determined
TEMPERATURE: 820.00°C PRESSURE: 500.00 bars
BULK: MASS: 100.25 g V: 39.65 cm3 DENSITY: 2.53 g/cm3 EFF. VISCOSITY: 8.00 log(poise)
G: -15575.46 J/g H: -13085.82 J/g S: 2.283 J/K-g Cp: 1.42 J/K-g

LIQUID: MASS: 65.76 g V: 27.46 cm3 DENSITY: 2.39 g/cm3 VISCOSITY: 7.42 log(poise) Giordano et al. (2007) LPSI
G: -16105.79 J/g H: -13481.76 J/g S: 2.41 J/K-g Cp: 1.58 J/K-g

LIQUID COMPOSITION (wt%):

SiO2	TiO2	Al2O3	Fe2O3	Cr2O3	FeO	MnO	MgO	CaO	Na2O	K2O	P2O5	H2O	CO2	S
54.027	0.653	24.181	0.542	0.000	0.238	0.198	0.051	5.644	5.892	6.501	0.351	1.722	0.000	0.000

SATURATED PHASES:
BULK MASS: 34.49 g BULK VOLUME: 12.19 cm3 BULK DENSITY: 2.83 g/cm3

PHASE	AFFINITY	MASS	TOTAL MASS	COMPOSITION			
Mt-Usp	0.00	3.426	3.43	mt	:0.9127	usp	:0.0873
Leucite (pure)	0.00	3.991	3.99	le	:1.0000		
HiCaPyroxene	0.00	9.999	10.00	di	:0.7062	hd	:0.2938
AlkaliFeldspar	0.00	14.485	14.48	or	:1.0000		
Nephaline(pure)	0.00	2.593	2.59	ne	:1.0000		

UNDERSATURATED PARTICIPATING MINERALS:

PHASE	AFFINITY	COMPOSITION
Apatite	2077.50	Pure phase